Deciphering the evolution of the Bleis Marscha rock glacier (Val d'Err, eastern Switzerland) with cosmogenic nuclide exposure dating, aerial image correlation, and finite- element modelling

Dominik Amschwand[1,3], Susan Ivy-Ochs[1,2], Marcel Frehner[1], Olivia Steinemann[2], Marcus Christl[2], Christof Vockenhuber[2]

[1]Department of Earth Sciences, ETH Zurich, 8092, Zurich, Switzerland
[2]Laboratory of Ion Beam Physics, ETH Zurich, 8093, Zurich, Switzerland
[3]Now at: Department of Geosciences, University of Fribourg, 1700, Fribourg, Switzerland

Correspondence to: Dominik Amschwand (dominik.amschwand@unifr.ch) ORCID: 0000-0003-2179-1481

Abstract. We constrain the Holocene ~~morphodynamic~~ development of the active Bleis Marscha rock glacier (Err-Julier area, eastern Swiss Alps) with ~~fifteen~~ 15 cosmogenic nuclide exposure ages (^{10}Be, ^{36}Cl), ~~2003/2012~~ horizontal surface creep rate quantification ~~from~~ by ~~orthophoto orientation correlation~~correlating two orthophotos from 2003 and 2012, and finite element modelling to separate the control exerted by topography and material composition on surface movement. ~~and semi-quantitative ice-content estimates from finite-element modelling. The results suggest that the complex Bleis Marscha rock glacier formed during two activity phases, one in the early Holocene and one in the late Holocene, separated by a mid-Holocene period of inactivation. The now transitional-inactive low-elevation lobes (first generation) formed after the retreat of the Egesen cirque glacier in a pulse-like manner at 11.5–9.0 ka. Rock-glacier viscosities inverted with the finite-element model hint at ground ice in these lobes which is possibly as old as its early Holocene debris cover. In contrast to the debris-conditioned rapid emplacement, the thermally controlled permafrost degradation is still ongoing, likely attenuated by thermal decoupling from the insulating coarse-debris boulder mantle. Nuclide loss from boulder erosion, affecting the nuclide inventory of boulders independently, led to a heterogeneous exposure age distribution on the transitional-inactive lobes. Exposure ages on such disturbed lobes record time elapsed since inactivation and are interpreted as (minimum) stabilisation ages. The inception of the active high-elevation lobes (second generation) at 2.8 ka is related to the late-Holocene cooling recorded at numerous sites across the Alps. Precise exposure ages of the last 1.2 ka correlate with down-stream distance and yield a long-term average surface speed coincident with 2003/2012 measurements. These long-term consistent surface creep rates indicate stable permafrost conditions and continuous rock-glacier growth despite the intermittent late-Holocene glacier cover of the Bleis Marscha cirque. The exposure ages on active, undisturbed lobes record time elapsed since boulder emergence at the rock-glacier root and are interpreted as travel-time estimates.~~ Bleis Marscha is a stack of three overriding lobes whose formation phases are separated by 'time gaps' expressed morphologically as over-steepened terrain steps and kinematically as sharp downslope decrease in surface movement. The three discrete formation phases appear to be correlated to major Holocene climate shifts: Early Holocene low-elevation lobes (~8.9–8.0 ka, after Younger Dryas), Middle Holocene

lobe (~5.2–4.8 ka, after thermal maximum), and Late Holocene high-elevation lobes (active since ~2.8 ka, coexisting with intermittent Bleis Marscha cirque glacierets). The formation phases appear to be controlled in the source area by the climate sensitive accumulation of an ice-debris mixture in proportions necessary for rock glaciers and susceptible to creep. Ongoing cohesive movement of the older generations requires ice at depth which is possibly as old as its early-/mid-Holocene debris mantle. Permafrost degradation is attenuated by 'thermal filtering' of the coarse debris boulder mantle, and implies that the dynamics of the Bleis Marscha lobes, that persisted over millennia once formed, are less sensitive to climate. The cosmogenic radionuclide inventories of boulders on a moving rock glacier ideally record time since deposition on the rock glacier root, but are stochastically altered by boulder instabilities and erosional processes. This work contributes to deciphering the long-term development and the past to quasi-present climate sensitivity of rock glaciers.

1 Introduction

Active rock glaciers are defined as "lobate or tongue-shaped bodies of perennially frozen unconsolidated material supersaturated with interstitial ice and ice lenses that move downslope or downvalley by creep as a consequence of the deformation of ice contained in them and which are, thus, features of cohesive flow" (Barsch, 1996). Their active phase and development are conditioned by ice preservation, permafrost conditions (Haeberli et al., 2006), and debris supply (Kenner and Magnusson, 2017).

In our current warming climate (Hock et al., 2019), active rock glaciers as the "visible expression of mountain permafrost" (Barsch, 1996) receive considerable attention. Their surface kinematics is considered as diagnostic for the thermal state of mountain permafrost (Delaloye et al., 2018), which is otherwise not directly observable. Rock glaciers are thought to store significant water resources ~~as ground ice~~ (Jones et al., 2019) and become more significant in the deglaciating mountains (Haeberli et al., 2017; Knight et al., 2019). However, in the literature, ~~contradicting~~ different views on the climate sensitivity of rock glaciers are proposed.

One concept is that rock glaciers respond attenuated and delayed to current warming because of the high thermal inertia of the ice-rich core and the thermal decoupling from external climate by the insulating effect of the boulder mantle (active layer) (e.g. Haeberli et al., 2017; Anderson et al., 2018) via the 'thermal semi-conductor' effect (Harris and Pedersen, 1998; Humlum, 1998; Hanson and Hoelzle, 2004~~; Guodong et al., 2007~~). The ground cooling effect of a ~~coarse debris~~coarse debris mantle (Schneider et al., 2012; Wicky and Hauck, 2017) favours a large negative thermal offset and permafrost conditions even at mean annual ground temperature (MAGT) close to 0 °C (Kellerer-Pirklbauer, 2019). Furthermore, the creep of millennia-old rock glaciers is tied to the ice-supersaturation of the debris and hence to the preservation of ~~ground ice~~ice over their entire lifetime (Barsch, 1996; Haeberli et al., 2003).

Another concept is the synchronous, rapid response to warming, based on kinematic ~~rock glacier~~rock glacier monitoring. ~~"Almost all~~Many rock glaciers across the Alps~~"~~ show a common behaviour of surface creep rates with (sub-)seasonal

fluctuations (Delaloye et al., 2010). These decennial to annual changes in surface creep rates respond within months to changing summer air temperature and snow cover timing (Noetzli et al., 2019). Rock glacier formation can occur within centuries (Humlum, 1996), or under very specific topo-climatic conditions even within decades (Scotti et al., 2017). Debris pulses or "surge packages" (Kenner et al., 2014), as well as "significant acceleration", ~~destabilisation~~ destabilization (Marcer et al., 2019) up to "sudden collapse" (Bodin et al., 2016) are reported. ~~Rock glacier formation can occur within centuries (Humlum, 1996), or under very specific topo-climatic conditions even within decades (Scotti et al., 2017).~~

~~Active rock glaciers are defined as "lobate or tongue-shaped bodies of perennially frozen unconsolidated material supersaturated with interstitial ice and ice lenses that move downslope or downvalley by creep as a consequence of the deformation of ice contained in them and which are, thus, features of cohesive flow" (Barsch, 1996). Their active phase and development are conditioned by ground ice preservation, permafrost conditions (Haeberli et al., 2006), and debris supply (Kenner and Magnusson, 2017). There are two paths to inactivity: (i) climatic inactivation and (ii) dynamic inactivation. In climatic inactivation ground ice melts out until its content falls below a critical saturation threshold where cohesive creep is no longer possible. The movement comes to a halt. This type of inactivation is a direct consequence of warming and a rising permafrost belt. In dynamic inactivation rock wall weathering rate and debris/ice incorporation becomes insufficient to sustain shear stresses required for the advancement, regardless of the rock-glacier thermal state and ground ice preservation. Ultimately, when ground ice is lost completely, the rock glacier deposit settles, although maintaining its diagnostic micro-topography. These former rock glaciers are defined as relict (Barsch, 1996).~~

The response of rock glaciers to external forcings such as air temperature, precipitation and snow cover, weathering intensity, debris supply, and interactions with glaciers (e.g. pushing ice, altered thermal conditions/insulation, glacial debris sources) are insufficiently understood. Furthermore, their external response is difficult to disentangle from internal thermo-mechanical and topographic feedbacks. Historical records are too short compared to typical rock glacier lifetimes, activity phases and response periods. ~~Long-term effects on rock glacier development must remain unresolved (Kenner and Magnusson, 2017).~~ To resolve long-term effects on rock glacier development (Kenner and Magnusson, 2017) and ~~To~~ to put the present-day morphology reflecting the lifelong dynamic history of active rock glaciers and (relict) rock glacier deposits ~~(Frauenfelder and Kääb, 2000)~~ in a climate- sensitivity context (Frauenfelder and Kääb, 2000), their activity phases need to be placed in a chronological framework. Cosmogenic radionuclide concentrations record all periods of exposure of the rock surface to cosmic rays. In principle, they are a suitable tool for deriving numerical exposure ages for boulders on the landform surface ~~Cosmogenic radionuclides exposure dating is a unique tool because it directly measures a chronometric, numerical exposure age of the landform surface~~ (Ivy-Ochs and Kober, 2008). The technique has been applied on (relict) rock glaciers deposits or related periglacial landforms by Ivy-Ochs et al. (2009), Böhlert (2011a, b), Moran et al. (2016), Denn et al. (2017, and references therein), and Steinemann et al. (2020). Relict and active ~~rock-glacier~~rock glacier deposits in Iceland were exposure dated by Férnandez-Férnandez et al. (2020).

In this study, our focus is on the Bleis Marscha rock glacier located in the Err-Julier area, eastern Swiss Alps (Fig. 1). ~~It is a 1100 m long, tongue-shaped rock glacier at an elevation range of 2400–2700 m a.s.l.~~ Previous relative dating studies based on Schmidt-hammer rebound values as well as thickness and chemical composition of weathering rinds suggest a Holocene-long development~~Previous studies used relative dating techniques~~ (Frauenfelder et al., 2001; 2005; Laustela et al., 2003). We exposure date 15 boulders along a longitudinal transect from the lowermost front up to the transition towards the talus with the cosmogenic radionuclides ^{10}Be and ^{36}Cl. This is the first study that exposure dates boulders on an active, presently moving rock glacier lobe in the Alps. The exposure ages are interpreted in light of field observations, ~~present~~ modern surface creep quantification through image correlation, and numerical finite~~-~~ element (FE) modelling to unveil periods of activity and the ~~morphodynamic~~ development of the Bleis Marscha rock glacier. This work contributes to deciphering the past to quasi-present climate sensitivity of rock glaciers in a high-mountain environment.

2 Study site

The studied Bleis Marscha rock glacier (WGS 84: 46°34′18″N, 9°42′~~10~~12″E; CH1903+ / ~~LV03~~LV95: 2'773'595, 1'160'326~~773553, 160325~~) lies on the eastern slope of the upper Val d'Err, a side valley of the Surses (Oberhalbstein) in the Err-Julier area, Grisons, eastern Swiss Alps (Fig. 1). The rock glacier originates in a NNW-~~facing~~ oriented cirque of Piz Bleis Marscha (3127 m a.s.l.).

The Err-Julier area lies in the rain shadow of the Lepontine, Bernese and Glarus Alps resulting in a dry-cold, continental-type climate. Frauenfelder et al. (2001) report low mean annual precipitation (MAP) of 900–1000 mm a^{-1} (1971–1990), a regional lapse rate of 0.55°C/100 m and a mean annual 0 °C-isotherm at c. 2180 m a.s.l. Val d'Err is a high valley with the valley floor at an elevation above 2000 m a.s.l. and surrounding peaks rising to over 3000 m a.s.l. The present-day lower limit of permafrost occurrence is roughly at 2400 m a.s.l. (Gruber et al., 2006; Boeckli et al., 2012).

The north-northwest to south-southeast oriented valley lies in a tectonically complex zone between the Upper Penninic Platta nappe overlain by the Lower Austroalpine Err nappe. The debris-supplying headwalls (in Tschirpen unit of the Err nappe) are composed of post-Variscan granitoids and Permo-Triassic to Lower Cretaceous sediments (mostly slate and carbonates), separated by a thrust outcropping subhorizontally along the cirque walls (Cornelius, ~~1935, 1950~~1932; Frauenfelder et al., 2005).

During the Last Glacial Maximum (LGM) around 24 ka (Ivy-Ochs, 2015~~; Wirsig et al., 2016~~), the area was covered up to an elevation of ~2800 m a.s.l. by ice flowing northwards from the nearby Engadine ice dome (Inn River catchment) into the Rhine glacier system (Bini et al., 2009). Prominent presumed Lateglacial (Egesen) moraines along the valley flanks (Schlosser, 1990; Frauenfelder et al., 2001) suggest that the upper Val d'Err, including our study site, was likely last occupied by a glacier during the Egesen stadial (12.9–11.7 ka (Ivy-Ochs, 2015)). The Bleis Marscha cirque was occupied by a glacieret during the Little Ice Age (LIA) and up until recently (Dufour, 1853; Frauenfelder et al., 2001).

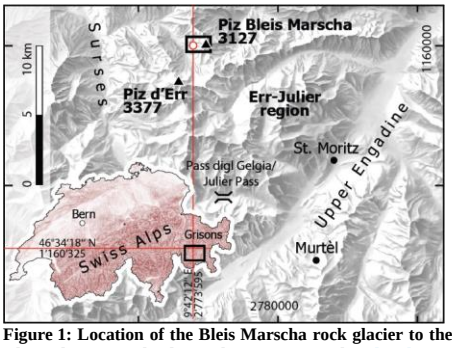

Figure 1: Location of the Bleis Marscha rock glacier to the west below Piz Bleis Marscha in the Err-Julier region, eastern Swiss Alps. The rectangle shows the area covered ~~in~~ by the geomorphological map (Fig. 3). Inset map: Location and extent (black rectangle) of the Err-Julier regional map within Switzerland and the coordinates of the lowermost front of the Bleis Marscha rock glacier (Maps reproduced with the authorization of the Swiss Federal Office of Topography swisstopo).

3 Material and Methods

Topographic maps, aerial photographs, digital elevation models, geomorphological field mapping, surface exposure dating, and finite element (FE) modelling form the data basis to reconstruct the Bleis Marscha development. The morphology of rock glaciers, where processes and form are intrinsically linked via deformation by creep, largely preserves the cumulative deformation history over the lifetime of the landform (cf. Frauenfelder and Kääb, 2000). The concept of rock glacier formation and the 'conveyor belt'-like advance mechanism form the theoretical groundwork on how surface boulders move compared to the rock glacier as a whole (outlined in Sects. 5.1–5.2). The subdivision in geomorphologically defined units of the polymorphic (sensu Frauenfelder and Kääb, 2000) Bleis Marscha rock glacier, assisted by an estimate of modern surface creep rates from aerial image correlation, provides a framework for the discussion and interpretation of the exposure ages. Surface exposure ages of 15 boulders of the rock glacier deposit were determined with the cosmogenic radionuclides ^{10}Be and ^{36}Cl. FE modelling separates the control of topography and material properties (e.g. ice content at depth) to the surface creep rate pattern.~~Topographic maps, aerial photographs, digital terrain models, geomorphological field mapping, surface exposure dating, and FEM were combined to reconstruct the development of the Bleis Marscha rock glacier.~~

3.1 Field work and Bleis Marscha landform analysis

Field mapping was performed in August 2017, focusing on Quaternary geology and geomorphology. Fieldwork was carried out at the scale of 1:5000 following standard geomorphological mapping procedures as outlined in Chandler et al. (2018). Details of the landforms and sediment of various sectors of the rock glacier were characterized to, in concert with digital

elevation model (DEM) analysis, subdivide it into different lobes. Especially distinguishing were lichen coverage (leading to pale vs. dark appearance of the blocks) and general freshness of the blocks, the location of ridges and furrows and the presence of steep steps in the rock glacier, as well as dominant size and rounding of blocks. Crosscutting relationships with talus and rockfall deposits, moraines and the past location of the cirque glacier were also examined based on historical maps. Landform interpretation was supported by aerial and DEM data in the iPad with Garafa GIS Pro application accessed in the field. Photos taken in the field and locations of boulders sampled for cosmogenic nuclide exposure dating were thus automatically georeferenced. ~~Fieldwork including mapping at a scale of 1:5000 and sampling was carried out in August 2017.~~ Orthorectified aerial images (0.25×0.25 m resolution) and the high-resolution ~~digital terrain model (DTEM)~~ "swissALTI3D" provided by the Swiss Federal Office of Topography (swisstopo) served for topographic analysis and ~~visualisation~~visualization. The ~~DTM~~DEM, acquired in 2016, is gridded on 2×2 m cells (resolution) and has an average error of ± 1–3 m (1σ level accuracy) for areas above 2000 m a.s.l. Extraction of swath profiles and morphometric calculations were carried out with the Matlab toolbox TopoToolbox 2 (Schwanghart and Scherler, 2014) and the open-source software QGIS.

3.2 ^{10}Be and ^{36}Cl exposure dating

~~The numerical ages of 15 boulders of the rock glacier deposit were determined with the surface exposure dating method using the cosmogenic radionuclides ^{10}Be and ^{36}Cl.~~

~~Ideally, the sampled rock surface has undergone undisturbed, single stage (no pre-exposure or inheritance), continuous exposure (no covering) in the same position (not shifted or toppled) since deposition (Ivy-Ochs and Kober, 2008).~~ Suitable boulders are large (>1.5 m side length) and in a stable position; suitable rock surfaces do not show signs of fast weathering or spalling. 15 ~~B~~boulders ~~at~~ on the rock glacier surface suitable for exposure dating were sampled with hammer, chisel, and battery-powered saw according to guidelines of Ivy-Ochs and Kober (2008) and field observations. Topographic shielding, dip, and dip direction of sampled surfaces were measured using a compass and clinometer. The samples (~0.5 kg of rock material each) were collected ~~along~~ close to the central flow line from the lowermost front up to the high-elevation active lobes, preferentially on ridges to minimise topographic and snow shielding (Böhlert et al., 2011b) and towards the frontal upper edge of each morphologically identified lobe (Haeberli et al., 2003; Steinemann et al., 2020). 14 samples were Julier granodiorite (quartz, ^{10}Be; Table 1); only one dolomite boulder for ^{36}Cl met the sampling criteria (Table 2).

^{10}Be sample preparation followed Kronig et al. (2018). The ratio of ^{10}Be/^{9}Be is measured with the 600 kV Tandy at the ETH Zürich Accelerator Mass Spectrometry (AMS) facility (Christl et al., 2013). The in-house standard S2007N, which is calibrated against the 07KNSTD was used. For ^{36}Cl extraction from the dolomite sample (Err8), the method of isotope dilution was employed (Ivy-Ochs et al., 2004). Concentrations of major and trace elements were measured by ICP-MS (Inductively Coupled Plasma Mass Spectrometry) at Actlabs (Ontario, Canada) (Table 3). AMS measurements were

conducted with the 6 MV Tandem accelerator (Synal et al., 1997; Vockenhuber et al., 2019) of the Laboratory of Ion Beam Physics, ETH Zurich.

The ^{10}Be surface exposure ages were calculated from the blank-corrected data (long-time laboratory blank of $^{10}Be/^{9}Be = (3.2 \pm 1.4) \times 10^{-15}$) using the CRONUS-EARTH online calculator (Balco et al. 2008) with the North-eastern North America (NENA) ^{10}Be production rate of 3.87 ± 0.19 atoms g^{-1} a^{-1} and the scaling model by Lal (1991)/Stone (2000). The shielding parameters were calculated with the "online calculators formerly known as the CRONUS-Earth online calculators" (Balco et al., 2008, http://hess.ess.washington.edu/math). The NENA production rate has been shown to be well applicable for the Alpine area (Claude et al., 2014). The ^{36}Cl surface exposure age was computed with an ETH Laboratory of Ion Beam Physics (LIP) in-house developed MATLAB program based on the equations and constants given in Alfimov and Ivy-Ochs (2009, and references therein). ^{36}Cl production in dolomite is dominated by spallation of Ca, muon interactions with Ca and low-energy neutron capture reflecting the high natural Cl concentration (Err8: 49.6 ± 0.1 ppm, Table 2). The following production rates were used: 48.8 ± 3.4 ^{36}Cl atoms g^{-1} a^{-1} for spallation in Ca and 5.3 ± 1.0 ^{36}Cl atoms g^{-1} a^{-1} for muon capture in Ca at the rock surface. A neutron capture rate of 760 ± 150 neutrons/g_{air} (Alfimov and Ivy-Ochs, 2009) was implemented. We used the Lal/Stone scaling of the production rates to the site latitude, longitude, and elevation (Balco et al., 2008).

~~The shielding parameters were calculated with the "online calculators formerly known as the CRONUS-Earth online calculators" (Balco et al., 2008, http://hess.ess.washington.edu/math).~~ We report and discuss exposure ages with an erosion rate of 1 mm kyr^{-1} for the crystalline samples (^{10}Be) and 5 mm kyr^{-1} for the dolomite sample (^{36}Cl). Snow-cover corrections are omitted as such corrections would ~~change~~ increase the exposure ages by only a few percent (by 6% for 50 cm of snow during 6 months a year). The reported errors are at the 1σ level including analytical uncertainties of the AMS measurements and the blank correction (internal errors).

3.3 Estimation of modern surface creep rates~~Orthophoto orientation correlation~~

We quantify the horizontal surface creep rate with the cross-correlation of orientation images (Fitch et al., 2002) derived from ~~bi-temporal~~two ortho-images with the Matlab tool ImGRAFT (Messerli and Grinsted, 2015). ~~The used~~ orthophoto mosaic *swissimage 25 cm* is a composite of orthorectified digital color aerial photographs, provided by the Swiss Federal Office of Topography (swisstopo). Ground resolution is given as 0.25 m, positional accuracy as ± 0.25 m. ~~We derived the orientation images from the R band of the RGB images.~~

The orientation correlation method developed by Fitch et al. (2012) is a feature-based method of translatory image matching that matches the orientation of the image intensity gradients. Orientation images are normalized and invariant to pixel brightness, making the method more robust and less susceptible to different illumination in the images. We derived the orientation images from the R band of the RGB images.

The post-processing steps are noise filtering to remove erroneous matches and smoothing to attenuate small-scale and thus likely short-lived ~~velocity~~ creep-rate variations. A minimum correlation coefficient of 0.6 and a conservative signal-to-noise ratio threshold ~~SRN_{min} =~~of 6 sufficed to remove incoherent and poor-quality displacement vectors. The optimal template size of 51×51 pixels was found using a procedure after Debella-Gilo and Kääb (2012). The search windows size of 211×211 pixels was defined with the recommendations of Messerli and Grinsted (2015). The modal displacement of the presumably stable adjacent off-rock glacier areas defined the significance level, that is the threshold below which any measured displacement is not distinguishable from immobility.~~We estimate the uncertainty by correlating a reference area in the valley floor considered as stable. The modal displacement defines the significance level, that is the threshold below which any measured displacement is not distinguishable from immobility.~~

~~Streamlines depict the trajectory and travel time for a particle travelling at the rock glacier surface, if the underlying surface flow field remains unchanged during the entire travel period (Kääb, Haeberli and Gudmundsson, 1997). Streamlines interpolated up-stream from the sampled boulders yield theoretical steady-state travel time estimates. We numerically integrate the defining ordinary differential equation with a Runge-Kutta 4th order scheme. Since streamline interpolation is noise sensitive, the input velocity field is additionally smoothed. Data gaps are interpolated with the Matlab tool "inpaint_nans" (D'Errico, 2012).~~

~~The horizontal surface deformation pattern is analysed by means of the strain-rate tensor (Kääb, Haeberli and Gudmundsson, 1997) defined as the symmetric part of the velocity gradient tensor. Velocity gradients are computed with the central finite difference scheme. Short-wavelength noise that lead to errors larger than typical strain rate values are filtered out by an additional circular averaging filter (low-pass) filter. The strain-rate orientation is visualised by the direction of the principal strain-rate axes, obtained via the diagonalization of the strain-rate tensor. In this particular representation of the strain rate tensor, the shear strain components vanish and the two non-zero components represent pure extension or contraction.~~

3.4 Finite~~-~~ element modelling

The surface movement of a rock glacier integrates the overall vertical deformation profile (~~Arenson~~ Müller et al., 2016). An appropriate flow law – a mathematical formulation of the governing deformation process – allows in principle to infer from (known, observable) surface properties to (unknown) effective material properties and structures at depth that cause the observed deformation.

The ~~long-term~~first-order deformation of rock glaciers is governed by gravity-driven steady-state creep of its ice-~~rich~~ bonded ~~core~~ interior (~~Arenson~~ Müller et al., 2016). In case of ice-supersaturation, the deformable (excess) ice leads to stress transfer in space and time and therefore to a ~~coherent~~ cohesive ~~velocity field~~surface creep rate pattern, a diagnostic feature of active rock glaciers. Creep of permafrost can ~~therefore~~ be approximately described by Glen's flow law for polycrystalline ice

(Haeberli et al, 2006), establishing a constitutive power-law relationship between shear stresses τ [Pa] and shear strain rates $\dot{\varepsilon}$ [s^{-1}]. The surface speed u_s [m s^{-1}] of an infinite, parallel-sided slab using Glen's flow law is

$$u_s = \frac{2A}{n+1}(\rho g \sin\bar{\alpha})^n H^{n+1}, \quad (1)$$

with flow rate factor A [Pa^{-n} s^{-1}] related to dynamic viscosity $\mu := \frac{\tau}{2\dot{\varepsilon}} = (2A\tau^{n-1})^{-1}$ [Pa s], stress exponent n [-], density ρ [kg m^{-3}], average surface slope $\bar{\alpha}$ [°], thickness H [m], and gravitational acceleration g [9.81 m s^{-2}]. However, Eq~~.~~ (1) is underdetermined, and no unique solution exists. A simultaneous determination of material properties (density, viscosity) and structure (thickness) is not possible. This inverse problem requires ~~regularisation~~ regularization to become solvable, i.e. all but one of these parameters need to be estimated independently.

The ~~rock glacier~~rock glacier model is mechanically described by the model parameters H, $\bar{\alpha}$, ρ, and μ. We invert for effective dynamic viscosity μ, from known surface slope $\bar{\alpha}$, and surface speed data u_s. We regularise the inverse problem by a-priori prescribing density ρ, and thickness H, parameters that can be reasonably well estimated from literature knowledge and field observations (Fig. 2a). In absence of any Bleis Marscha rheological borehole data to constrain the power-law exponent n of the effective viscous flow law, we proceed by a forward operator that implements the simplest temperature-independent (isothermal) linear viscous (Newtonian) material ($n = 1$). The system of force-balance and ~~isothermal~~ constitutive equations are solved numerically in two dimensions with the numerical FE code presented in Frehner et al. (2015).

Direct evidence from over-steepened rock glacier fronts, borehole deformation measurements (Arenson et al., 2002) and indirect geophysical investigations (Springman et al., 2012) suggest a pronounced thermo-mechanical layering of rock glaciers. A robust finding is that the deforming part can be divided into a sequence of three layers, surface boulder mantle, rock glacier core, and shear layer (Haeberli et al., 2006; Frehner et al, 2015; Cicoira et al., 2020). (1) The seasonally frozen ice-free/poor surface layer consists of a matrix-poor, clast-supported framework of large, interlocked boulders (~active layer). Discrete movements of blocks in the boulder mantle are negligible compared to the total surface movement (but not with respect of inventories of cosmogenic nuclides, cf. Sect. 5.2). Deformation is accommodated by the ice-bearing interior that comprises the rock glacier core and the basal shear layer. (2) The ice-rich rock glacier core consists of a of a perennially frozen mixture of ice, debris, and fine material. (3) A fine-grained, few meters thick shear layer concentrates 60-90% of the total displacement. Its higher deformation susceptibility, arising from the weakening effect of liquid water at grain boundaries, is in the model accounted by a lower viscosity. Boulder mantle, core and shear layer lie on an immobile substratum of debris or bedrock. ~~Direct evidence from over-steepened rock glacier fronts, borehole deformation measurements (Arenson et al., 2002) and indirect geophysical investigations (Springman et al., 2012) suggest a pronounced mechanical layering of rock glaciers. A robust finding is a sequence of three main layers (Haeberli et al., 2006; Frehner et al, 2015). (1) The ice-free surface layer consists of a matrix-poor, clast-supported framework of large, interlocked boulders. (2) Beneath the boulder mantle, the ice-rich permafrost layer consists of a frozen mixture of ice, debris, and fine material.~~

~~This rock-glacier core accommodates the horizontal deformation, often concentrated in localized shear zones or décollements. (3) Boulder mantle and core lie on a stiff, immobile substratum of ice-poor, frozen debris, which does not contribute to the observed dynamic deformation of the rock glacier (Arenson et al., 2002).~~ Over-steepened terrain steps, exposing the uppermost few meters of the stratigraphy, show the coarse boulder mantle over the finer-grained rock glacier core (cf. field observations in Sect. 4.1). Although no borehole deformation data is available for Bleis Marscha that could evidence the shear layer, we are confident that this typical rock glacier feature does exist there. ~~Field observations suggest that the general rock-glacier stratigraphy is valid for the studied Bleis Marscha rock glacier (Sect. 4.1).~~ We approximate the deforming~~, dynamic~~ part of the rock glacier as a three-layer system consisting of a 5 m thick boulder mantle ~~(constant along profile)~~, ~~~~30~~ ~~50~~ 40 m thick core ~~(variable)~~ and a 3 m thick basal low-viscosity shear ~~zone~~ layer~~(constant)~~. The (variable) ~~cumulative~~ total thickness is estimated as follows: The model top boundary is the ~~rock-glacier~~rock glacier surface given by the ~~DTM~~DEM, implemented as a free surface (Fig. 2b). The bottom boundary is defined by a fixed, no-slip boundary to the immobile substratum. Its elevation is projected from the adjacent terrain at the ~~rock-glacier~~rock glacier front where the rock glacier rises from the Salteras ~~terrace~~ trough shoulder (Fig. 2a; cf. Kääb and Reichmuth, 2005; Scapozza et al., 2014) and parallel to the average ~~rock-glacier~~rock glacier surface in the upper stretches. All layers including the ice-free boulder mantle effectively obey a viscous flow law and are separated by no-slip boundaries (dynamically coupled, "welded") (Arenson et al., 2002; Springman et al., 2012; Frehner et al., 2015).

We estimate the density of the rock glacier materials as the weighted average of the density of its constituents (Müller et al., 2016), namely debris (~~Err granodiorite~~Err Granodiorite, ρ_{debris} = 2700 kg m^{-3}), ice (ρ_{ice} = 910 kg m^{-3}), and air (ρ_{air} = 1 kg m^{-3}) ~~(Eq. 10 in Müller et al., 2016)~~. For the approximately void-free ~~rock-glacier~~rock glacier core with 60 vol% ice, we obtain ρ_c = 1626 kg m^{-3}, and for the ~~ice-free~~ boulder mantle with 30 vol% air ρ_m = 1890 kg m^{-3} (Barsch, 1996; Fig. 2b). The effect of water on density is insignificant. The prescribed viscosity ratios between the different layers are: ~~rock-glacier~~rock glacier core to high-viscosity boulder mantle 1:20 (estimated from dominant wavelength of furrow-and-ridge microtopography, cf. back-of-the-envelope calculation below~~Sect. 4.1~~; Fig. 2b), and core to low-viscosity basal shear layer 10:1 (conservative ~~estimate~~assumption from the literature, cf. Cicoira et al. (2020) and references therein~~; Fig. 2b~~). To estimate the effective viscosity ratio R between the rock glacier mantle and core, we use an analytical formula based on buckle-folding theory that we apply to the furrow-and-ridge microtopography on units I–II (cf. Sec. 4.1; equation modified for one-sided support from Biot (1961); cf Frehner et al., (2015)):

$$R := \frac{\mu_m}{\mu_c} = \frac{3}{8}\left[\frac{\lambda_d}{\pi h_m}\right]^3. \quad (2)$$

The viscosity ratio R can be calculated from the dominant wavelength λ_d and rock glacier mantle thickness h_m. Inserting λ_d = 50 m and h_m = 4 m (estimates from field observations), we roughly estimate R = 24.

The susceptibility for steady-state creep of debris-ice mixtures depends on debris-ice proportions (specifically the degree of ice supersaturation, i.e. the ice volume exceeding the pore volume), fabric, particle size, temperature and water content (Moore, 2014). Since the influence of each parameter is difficult to disentangle and the material properties and composition are not known at this level of detail, we absorb these contributions by the effective viscosity, μ, and estimate it by solving the inverse problem. We depart from an initial ~~rock-glacier~~rock glacier model with a uniform viscosity of pure ice for the entire ~~rock-glacier~~rock glacier core, $\mu_c^0 = 2 \times 10^{13}$ Pa s as an initial guess. Next, we compute synthetic surface velocity data by means of the discretized forward operator, carried out by the numerical FE code (Fig. 2c). The synthetic data predicted by the current model is visually compared to the measured data, the orthophoto-derived surface creep rates. For ~~rock-glacier~~rock glacier parts where the misfit between synthetic/predicted and measured data exceeds the data uncertainty, the viscosity is either increased if synthetic velocities were too high compared to measured values ($d_{pred} > d_{meas}$) or decreased in the opposite case ($d_{pred} < d_{meas}$, estimation problem). The obtained plausible ~~rock-glacier~~rock glacier viscosity distribution, $\tilde{m}$, that explains the measured surface velocities, d_{meas}, within their uncertainty, is one solution to the inverse problem.

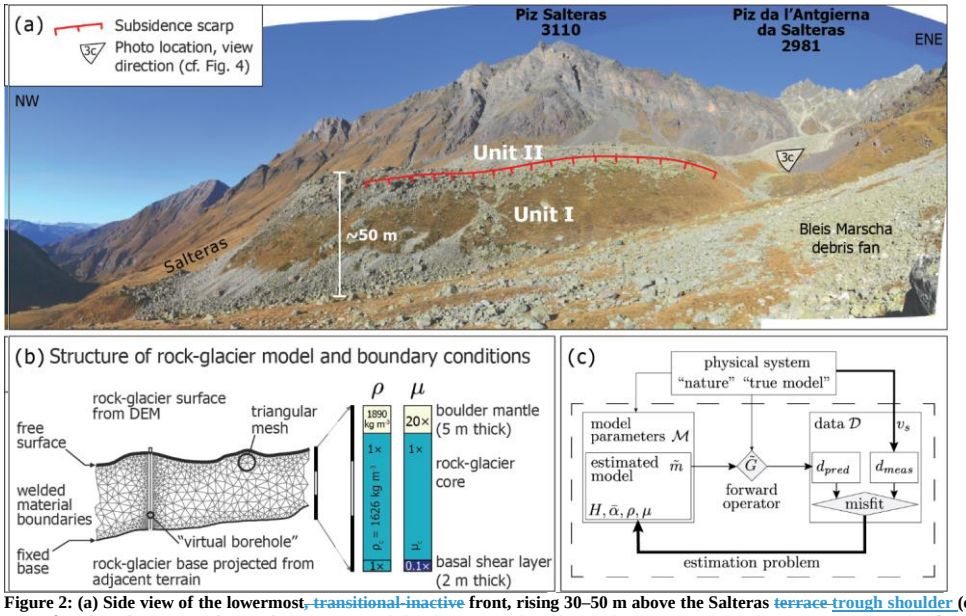

Figure 2: (a) Side view of the lowermost~~, transitional-inactive~~ front, rising 30–50 m above the Salteras ~~terrace~~ trough shoulder (cf. Fig. 4 for photo location and view direction). A stabilized, grassy sidewall extends upstream beneath younger lobes. ~~Part of t~~The southernmost ~~front~~ fringe is subsiding, possibly due to ~~ground ice~~ice loss. ~~The vertical throw of the subsidence scarp is 2–3 m.~~ (b) Finite element (FE) model setup, triangular mesh (Shewchuk, 1996), boundary conditions, and prescribed ratios of density ρ and

dynamic viscosity μ (profiles). The surface boundary is the well-constrained elevation along a longitudinal profile, extracted from the ~~DTM~~ DEM as a swath profile with TopoToolbox. The a-priori prescribed density and viscosity ratios create the characteristic mechanical layering of rock glaciers with a stiff, high-viscosity boulder mantle, deformable core, and basal weak, low-viscosity layer. (c) Inverse problem structure with the model parameters that are linked to the observable data via the forward operator $\tilde{G}$, the FE model. The model predicts a synthetic surface velocity from the mechanical parameters that control the ~~rock glacier~~rock glacier creep: thickness H, average surface slope $\bar{\alpha}$, density ρ, and dynamic viscosity μ.

4 Results and interpretation~~: Geomorphology, age, and kinematics of the Bleis Marscha rock glacier~~

4.1 ~~Field observations~~Geomorphology of Bleis Marscha

The Bleis Marscha rock glacier is a tongue-shaped multi-unit or polymorphic (sensu Frauenfelder and Kääb, 2000) talus rock glacier at an elevation range of 2400–2700 m a.s.l. (Fig. 3). With a length of 1100 m, a width of 150–200 m, a surface area of ~2.4 × 10^5 m^2, and a source area of ~3.1 × 10^5 m^2, it ranks among the largest rock glaciers in the Err-Julier area. Based on an assumed mean thickness of 30-40 m, ~~We~~ we estimate a total volume of ~(7–10) × 10^6 m^3. ~~Internal steep frontal scarps~~

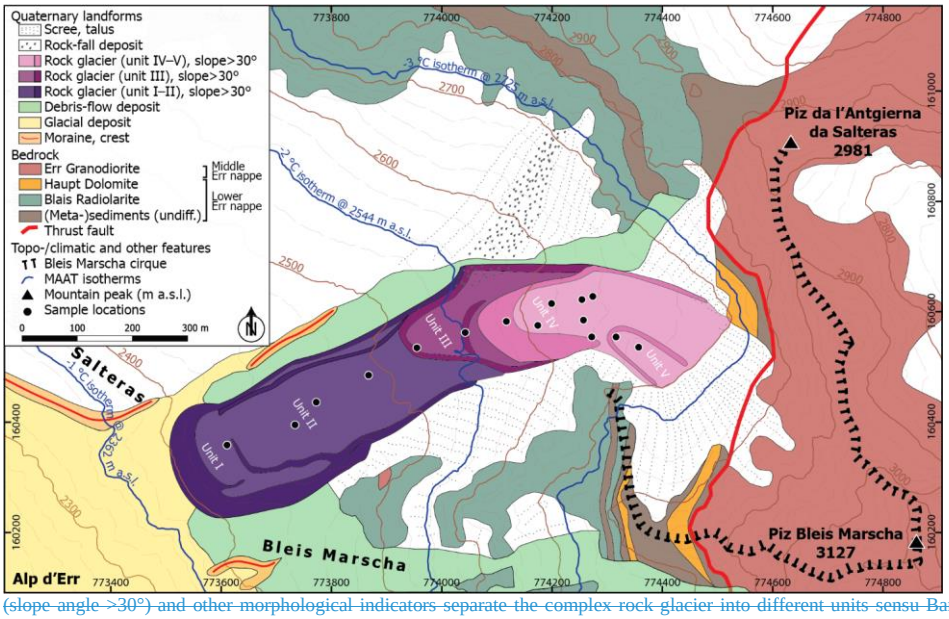

~~(slope angle >30°) and other morphological indicators separate the complex rock glacier into different units sensu Barsch (1996), each apparently with its own activity phase and status. We subdivide the Bleis Marscha rock glacier into a two-part sequence comprised of two active upper lobes (units IV–V; 2550–2700 m a.s.l.) that override three transitional to inactive lower lobes (units I–III; 2400–2550 m a.s.l.; Figs. 3, 4).~~

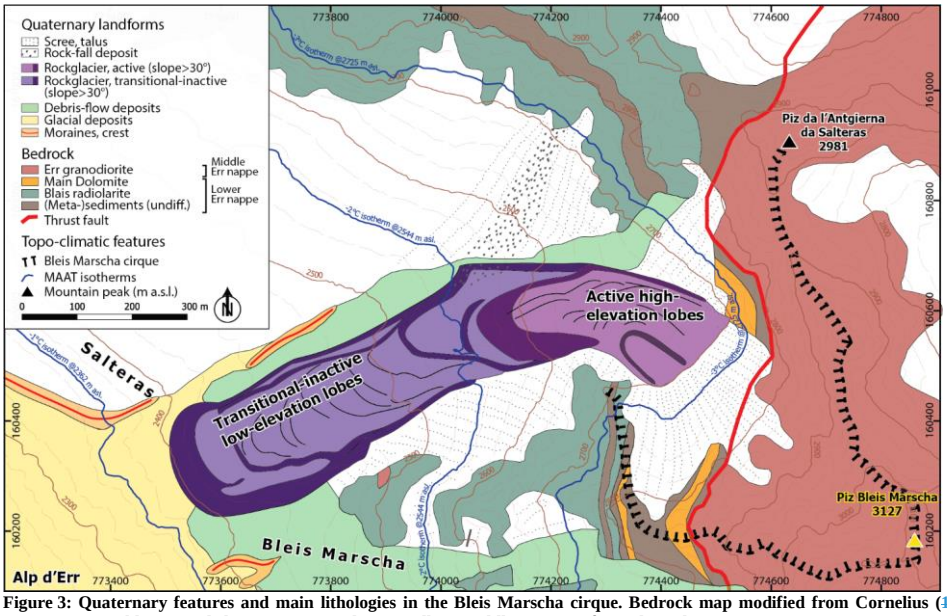

Figure 3: Quaternary features and main lithologies in the Bleis Marscha cirque. Bedrock map modified from Cornelius (~~1935, 1950~~1932). A subhorizontal thrust separates the crystalline Middle Err unit from the sedimentary Lower Err unit. Present-day MAAT isotherms are drawn according to Frauenfelder et al. (2001).

The rock glacier boulder mantle consists of three main rock types, each with its ~~well-localised~~ source in different parts of the cirque headwall (Fig. 3, Cornelius (~~1935, 1950~~1932)): prevalently weathering-resistant ~~Err granodiorite~~Err Granodiorite, followed by ~~Blais radiolarite~~Blais Radiolarite and tectonically fractured ~~Main~~ Haupt ~~dolomite~~Dolomite. Weathering-prone lithologies such as rauhwacke (cellular dolomite), conglomerate, limestone and shales occur only in lenses or thin seams in the headwall and are only rarely found on the ~~rock-glacier~~rock glacier surface. ~~The angular blocks have typical volumes of~~Block volumes are typically between 0.5–50 m^3~~,~~. Average block diameter is 1–2 m, exceptionally with >10 m edge length. Size of the largest blocks increases in the direction of the rock glacier front. Downstream, the rock glacier rises over and is disconnected from the surrounding terrain.~~The dominance of Err granodiorite (>80 vol%) increases towards the lowermost front. Therefore, the lower lobes were originally connected to the talus and must extend upslope beneath the now-active lobes. Weathering-prone lithologies such as rauhwacke (cellular dolomite), conglomerate, limestone and shales occur only in lenses or thin seams in the headwall and are only rarely found on the rock-glacier surface. The rock glacier coarse-debris transport system is downstream disconnected from the laterally adjacent terrain.~~

Observations such as overall debris color reflecting differences in freshness of the sediment (weathering of the granite and lichen coverage), degree of soil development and internal steep frontal terrain steps (slope angle >30°) allowed us to subdivide the complex rock glacier into five different morphological units (Fig. 3) sensu Barsch (1996). These are labelled unit I (the lowest elevation, frontal part) to unit V (the highest elevation lobe). We interpret terrain steps as marking internal boundaries in the rock glacier related to overriding of lower lobes by higher lobes. The lower lobes must originally have been connected to the talus slopes in the Bleis Marscha cirque, the only source of Err Granodiorite, as testified by the dominance of Err Granodiorite (>80 vol%) increasing towards the lowermost rock glacier front. No large enough glacier existed throughout the Holocene to move debris out of the cirque. In theory, the lower lobes in part underlie the overriding higher lobes. Along its lower part (units I–II), the rock glacier lies on a till-mantled bedrock step (trough shoulder) known as Salteras. Schlosser (1990) mapped a right-lateral moraine near the trough shoulder break in slope (Fig. 3) and interpreted it as belonging to the Egesen stadial. The moraines and the rock glacier are nowhere in contact.

The lowermost front of the Bleis Marscha rock glacier rises roughly 30–50 m from edge of the Err valley trough shoulder at an elevation of 2380 m a.s.l. (Fig. 2a). The frontal part, denoted as unit I (Figs. 3, 4), exhibits several features suggesting that it is apparently inactive (cf. Sect. 4.3). This includes signs of settling thus incipient degradation of the rock glacier body, patches of vegetation and marked soil development, as well as extensive lichen cover, iron staining and weathering rinds. Yet, a frontal boulder apron indicates that the movement of this apparently old body has not ceased completely. The boundary between unit I and II is a steep, ca. 2–3 m high terrain step, that extends upstream as a stable, grassy sidewall along the two lobes (margin of unit I, Fig. 2a). Where unit II rests on unit I, it is recessed by ~5 m forming a ledge along the sides (Fig. 5c). The boulder weathering and abundance of black and green lichen give the lower lobes (units I–II) a much darker brownish grey appearance in comparison to the higher elevation lobes. Blocks in units I–II are subangular to subrounded; weathering of the Err Granodiorite blocks plays an important role. The surface of unit II is gently inclined (~10°), with a well-developed furrow-and-ridge microtopography of down-stream crescent-shaped transverse ridges that are regularly spaced about 50 m apart and separated by <5 m deep furrows (Fig. 5b). The mean rock glacier surface slope and presumably also the basal slope steepens from ~10° to 20° at an elevation of 2500 m a.s.l., causing units I–II to decelerate. The break in slope induced along-flow compressive stresses (Fig. 5b). Buckle folding of the layered rock glacier (stiff boulder mantle, deformable ice-rich core) in response to compressive flow likely was the dominant formation mechanism of the transverse furrow-and-ridge microtopography of unit II (cf. Frehner et al., 2015; Sect. 3.4).

Along the left-lateral side of units I–II, a WSW-ENE running scarp indicated by exposed fresh material dissects both units and is therefore a younger feature. The southernmost fringe of the rock glacier is slowly subsiding. Debris slides or aprons do not follow along the entire scarp. The slow, interior deformation must originate at depth rather than at shallow levels, what would push loose surface debris over the edge. The body is sagging instead of laterally advancing, for which ice loss is a possible explanation.

Unit III is clearly differentiated from units I–II by the slightly paler color of the debris (less brown) and by a steep, 5 m high, frontal terrain step (Fig. 5b). This terrain step is quite marked; the grass cover and soil development suggest long-term stability. The incipient soil development and vegetation patches, clearly differentiate unit III from the upper units IV and V. The right-lateral boulder apron along unit III between the rock-fall deposits and its front formed by debris slides pours fresh material over a stabilized, grassy sidewall, which suggests recent activity of unit III (Fig. 5c). Units I–III are bordered by a stable lateral ridge which is densely vegetated and has a thick soil cover (Figs. 5b, c). It extends upslope until the body disappears beneath the younger unit IV (Fig. 2a). We interpret this grassy ridge as the margin of the oldest, possibly relict body (unit I) that underlies the younger lobes (units II and III), and not as lateral moraines (Frauenfelder et al., 2001; cf. Barsch 1996).

The boundary between unit III and IV is another steep 5 m step in the terrain. The steep (>20°) terrain here is cut by three major scarps where the two-layered stratigraphy of a coarse, clast-supported blocky mantle (thickness of ~3 m) over a finer, matrix-supported core is exposed. These inner terrain steps are expressions of discontinuities and form the frontal boundary of units III and IV (Fig. 5b). Units IV–V are starkly different in appearance from units I–III. Again, the hue of the debris lightens (more grey than brown), the debris is much less weathered, boulders are more angular. The maximum block size decreases from 5–6 m in diameter to 2–3 m. Vegetation and soil patches are lacking. Unit IV exhibits several longitudinal ridges along the right-hand side (Fig. 4). In the bend at the lip of the cirque, the microtopography becomes more accentuated with a set of parallel longitudinal, asymmetric ridges (steep side facing outwards), whose amplitude however rarely exceeds 2 m. These are flow features that likely relate to the left turn that the rock glacier makes here. Unit V, a small rock glacier lobe (width 80 m), is well visible in the root zone emanating from the talus slope (Figs. 4, 5a).

We observed neither signs of glacier activity nor any surface ice remaining from the recent glaciation of the cirque (Dufour, 1853; Siegfried, 1887). The “small ice patch” mentioned by Frauenfelder et al. (2005) was no longer visible in 2017. The smooth, unstructured talus passes directly into the broad (180 m) rock glacier root zone (unit IV) at an elevation of 2700 m a.s.l. (Fig. 5a). No morphological evidence of the recent LIA glacier remains.

~~Despite the very recent glaciation of the cirque (1853 Dufour, 1887 Siegfried maps: Dufour, 1853; Siegfried, 1887), we did not observe signs of glacier activity nor any surface ice. The small ice patch mentioned by Frauenfelder et al. (2005) had completely disappeared by 2017. The smooth, unstructured talus passes directly into the broad (180 m) rock glacier root zone (unit IV) at an elevation of 2700 m a.s.l. (Fig. 5a). No geomorphological evidence of the LIA glacier remains. A small rock glacier lobe (unit V, width 80 m) is well visible in the root zone emanating from the talus (Fig. 4). In the bend at the lip of the cirque, the micro-topography becomes more accentuated with a set of parallel longitudinal, asymmetric ridges (steep side facing outwards), whose amplitude however rarely exceeds 2 m. This lobe rests on an older, apparently inactive body (unit III, Fig. 5a) that displays incipient soil development, vegetation patches and a most likely rock fall-derived radiolarite-debris covered protrusion (Fig. 5a). The steep (>20°) terrain is cut by three major scarps where the two-layered stratigraphy~~

of a coarse, clast-supported blocky mantle (thickness of 3–5 m) over a finer, matrix-supported core is exposed. These inner scarps are expressions of faults and form the frontal boundary of units III and IV (Fig. 5b). The right lateral boulder apron along unit III between the rock fall deposits (protrusion) and its front formed by debris slides exposing fresh material suggests recent movement despite morphological signs of inactivity (Fig. 5c).

Unit II (the one being overridden by unit III) appears distinctly older and inactive. The lobe is marked by signs of settling and weathering such as vegetation patches, lichen-covered boulders, iron staining, weathering rinds and a frontal apron. The surface is gently inclined (10°), with a well-developed furrow-and-ridge micro-topography of crescent-shaped transverse ridges separated by <5 m deep furrows (Fig. 5b). The lobe rests on an older, inactive to possibly relict body (unit I), recessed by ~5 m and forming a ledge along the sides (Fig. 5c). The transitional-inactive lowermost lobes (units I–III) are bordered by a stable outer ridge which is densely vegetated and has a thick soil cover (Figs. 5b, c). It extends upslope until the body disappears beneath the younger unit IV (Fig. 2a). We interpret this grassy ridge as the margin of the oldest, possibly relict body (unit I), and not as lateral moraines (Frauenfelder et al., 2001; cf. Barsch 1996). The front of unit I, mantled by a fall-sorted boulder apron, rises roughly 30–50 m from the edge of the Salteras terrace at an elevation of 2380 m a.s.l. (Fig. 2a). This lowermost front of the Bleis Marscha rock glacier has come to a halt just at the edge of the trough shoulder with a (Egesen?) moraine ridge. The moraines and the rock glacier are nowhere in contact (Fig. 3).

A WSW-ENE running scarp, indicated by exposed fresh material, dissects both units I and II and is therefore a younger feature (Figs. 4, 2a). A part of the lowermost lobes (300 m × 30 m) is slowly collapsing and subsiding southwards, perpendicular to the former creep direction. No bulges, debris slides or debris aprons are observed, i.e. the deformation must be slow and distributed. The body is sagging instead of laterally advancing, which hints at ground ice loss.

The mean surface slope and presumably also the basal slope drops from 20° to 10° at an elevation of 2500 m a.s.l., causing the lower lobes to decelerate and to buttress against the upper lobes. The break in slope induced along-flow compressive stresses (Fig. 5b). Buckle folding of the layered rock glacier (boulder mantle, ice-rich core) in response to compressive flow likely was the dominant formation mechanism of the transverse furrow-and-ridge micro-topography in the lower part (cf. Frehner et al., 2015). We use an analytical formula for the effective viscosity ratio R between the rock glacier mantle and core (equation modified for one-sided support from Biot (1961)):

$R := =$. (2)

The viscosity ratio R can be calculated using the dominant wavelength and rock glacier mantle thickness . Inserting = 54 m obtained via Fourier analysis and = 4 to 5 m, we estimate R = 30 to 15.

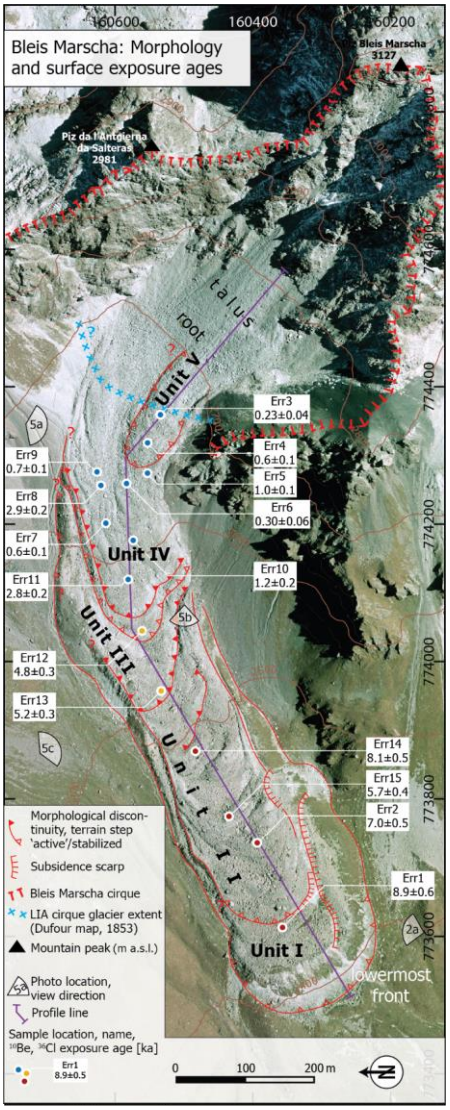

Figure 4: Plan view of morphological domains on 2003 orthophoto showing the morphological discontinuities (inner fronts~~,~~ /~~scarps~~terrain steps, slope breaks), sampling locations and exposure ages (~~uncertainties are internal errors; (~~cf. Fig. ~~7~~ 8 for ~~kinematic domains~~surface creep rates). Bleis Marscha is a stack of three overriding lobes composed of units I–II, unit III, and units IV–V, separated by terrain steps. ~~Units I–III are transitional inactive lobes overridden by the active units IV–V.~~ Historical maps suggest that the Holocene maximum extent of the cirque glacier, ~~extent~~ reached during the Little Ice Age (LIA) around CE 1850, remained within the Bleis Marscha cirque. (Orthophoto reproduced with the authorization of the Swiss Federal Office of Topography swisstopo).

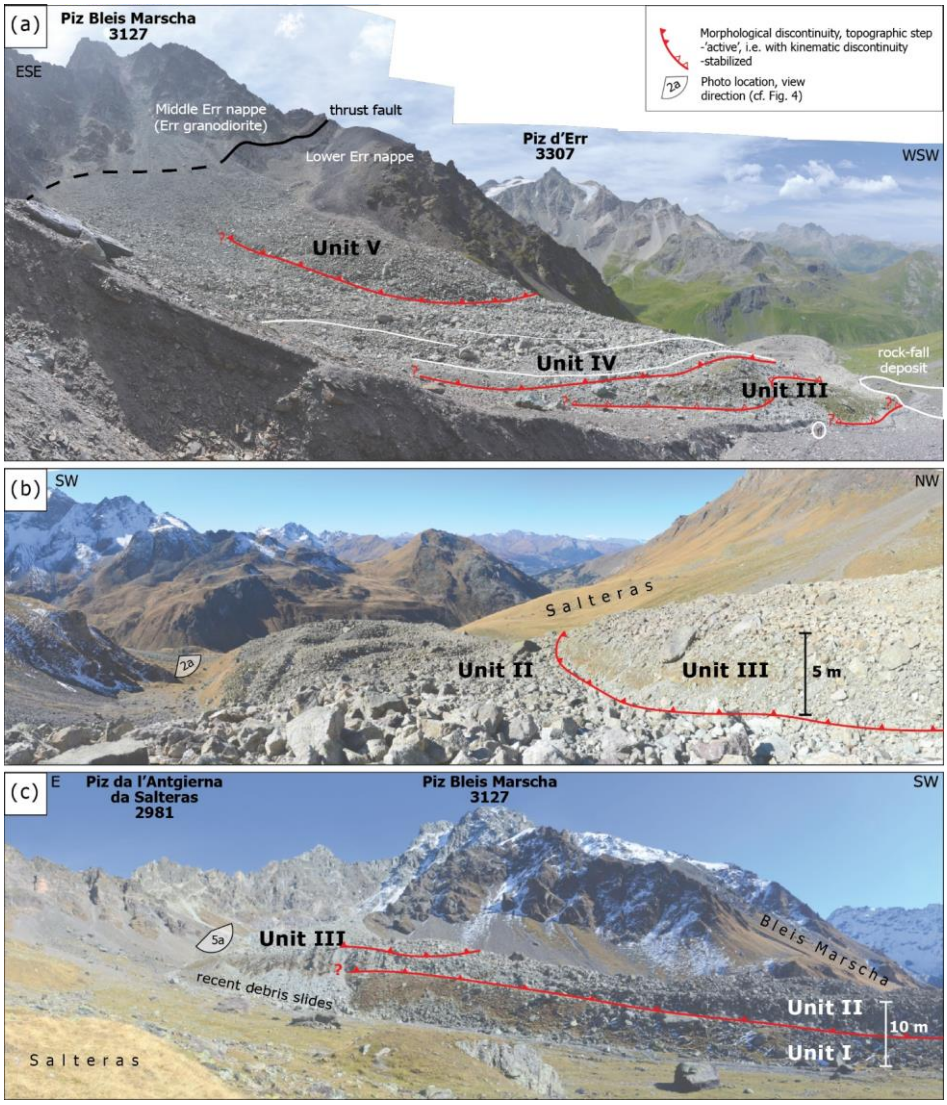
(a)
Piz Bleis Marscha
3127
ESE
Middle Err nappe
(Err granodiorite)
thrust fault
Lower Err nappe
Piz d'Err
3307
WSW
Morphological discontinuity, topographic step
-'active', i.e. with kinematic discontinuity
-stabilized
Photo location, view
direction (cf. Fig. 4)
Unit V
Unit IV
Unit III
rock-fall
deposit
(b)
SW
NW
Salteras
Unit II
Unit III
5 m
(c)
E
Piz da l'Antgierna
da Salteras
2981
Piz Bleis Marscha
3127
SW
Unit III
recent debris slides
Bleis Marscha
Unit II
10 m
Unit I
Salteras

Figure 5: Panorama images of the Bleis Marscha rock glacier (cf. Fig. 4 for photo locations). (a) View to SE into the root zone in Piz Bleis Marscha cirque. The dominant lithology of the boulder mantle, Err Granodiorite, ~~Most of the rock glacier material~~ is sourced above the thrust fault in the back of the cirque ~~from the crystalline Middle Err nappe (Err granodiorite outcropping above thrust fault). Note the debris-filled cirque with the prograding talus slope (transport-limited system) and the sudden terrain drop-off just below the cirque lip~~. Photo taken in August 2018. (b) View to W onto lower ~~rock glacier~~rock glacier part with furrow-and-ridge ~~micro-topography~~microtopography (unit II). The currently advancing unit III is outlined by the prominent ~~inner scarp~~terrain step. Photo taken in October 2018. (c) Side view to SE of the middle ~~rock glacier~~rock glacier part, evidencing the Bleis Marscha rock glacier as a multi-unit debris stream composed of multiple stacked lobes. The fresh lateral debris apron ~~along the orographic right side of~~along unit III hints at ongoing activity ~~and likely recent reactivation~~. Unit I at the base of the stack is discernible by the ~~vegetated,~~ stable, ~~outer ridge~~grassy sidewall and the ledge beneath unit II. Photo taken in October 2018 . ~~The different coloring and composition of the autumnal vegetation is related to the substrate lithology: While the brownish grass in the foreground (moraine ridge, likely Egesen stadium of Bleis Marscha cirque glacier) grows on Err granodiorite, the depression between the rock glacier and the parallel-running moraine is filled with down-washed fines of mostly Blais radiolarite, schists and carbonates (higher moisture retention capacity).

4.2 Boulder exposure ages

~~The m~~Measured ^{10}Be concentrations are in the range of (0.7 ± 0.1 to 23.6 ± 1.2) × 10^4 at g^{-1}~~,~~. ~~the~~ The measured ^{36}Cl concentration is (3.1 ± 0.1) × 10^5 at g^{-1} (Tables 1, 2). ~~The c~~Cosmogenic nuclide exposure ages (^{10}Be and ^{36}Cl) range from 0.23 ± 0.04 ~~ka~~ to 8.95 ± 0.~~47~~ 64 ka (Figs. 4, ~~6~~7; Tables 1, 2).

~~Two distinct age populations are distinguished: (i) a late Holocene group with precise ages ranging from 0.2 to ~1.2 ka located on the high-elevation active rock glacier lobes (samples Err3, 4, 5, 6, 7, 9, 10), and (ii) an early-to-middle Holocene group with dispersed (overlapping ±1σ range) ages ranging from ~4.8 to ~9.5 ka on the lower inactive lobes (samples Err1, 2, 12, 13, 14, 15). The ^{10}Be and ^{36}Cl ages of Err11 and Err8, respectively, defy this first-order classification.~~

For the lowermost, oldest part of the rock glacier (unit I), we obtained one ^{10}Be exposure age: Err1 at 8.95 ± 0.64 ka (Figs. 4, 6a, 7). The three ages for unit II are, from lowest elevation to highest, 7.03 ± 0.51 ka (Err2, Fig. 6b), 5.70 ± 0.40 ka (Err15, Fig. 6c) and 8.08 ± 0.46 ka (Err14, Fig. 6d). From the next higher unit III, we obtained two ^{10}Be ages: 5.17 ± 0.35 ka (Err13, Fig. 6d) and 4.80 ± 0.33 ka (Err12, Fig. 6e). In the higher elevation, more active parts of the Bleis Marscha rock glacier, nine ages were determined, seven from unit IV and two from unit V. The ^{10}Be ages for unit IV are from lower to higher elevation, Err11 at 2.77 ± 0.17 ka (Fig. 6f), Err10 at 1.18 ± 0.16 ka, Err7 at 0.65 ± 0.06 ka, Err6 at 0.30 ± 0.06 ka, Err9 at 0.73 ± 0.08 ka and Err5 at 1.00 ± 0.08 ka. The ^{36}Cl age for a dolomite boulder in unit IV is 2.89 ± 0.18 ka (Err8, Fig. 6g). The ages from the highest youngest lobe, unit V, are 0.56 ± 0.06 ka for Err4 and 0.23 ± 0.04 ka for Err3 (Fig. 6h).

Ages generally decrease from the lowermost toe of the rock glacier (unit I) to the uppermost lobe (unit V). Nevertheless, ages on different morphological units show a degree of ‘geologic scatter’. In stark contrast to nearly all exposure dating projects whereby the cosmogenic nuclide concentration records the time elapsed since the boulder has reached its final position (e.g. on a moraine or a landslide deposit), we have dated an active, moving landform. This requires a different way of looking at the exposure dates. The cosmogenic nuclide concentrations comprise all the nuclides acquired during exposure of the sampled surfaces. This includes in the bedrock (inheritance), at the talus foot, on the rock glacier surface including

while it is moving and at the final boulder position. Effects already discussed in other studies (Heyman, 2011) such as boulder rolling, toppling or spalling can also affect the nuclide concentration. This is discussed in detail in Sect. 5.2.

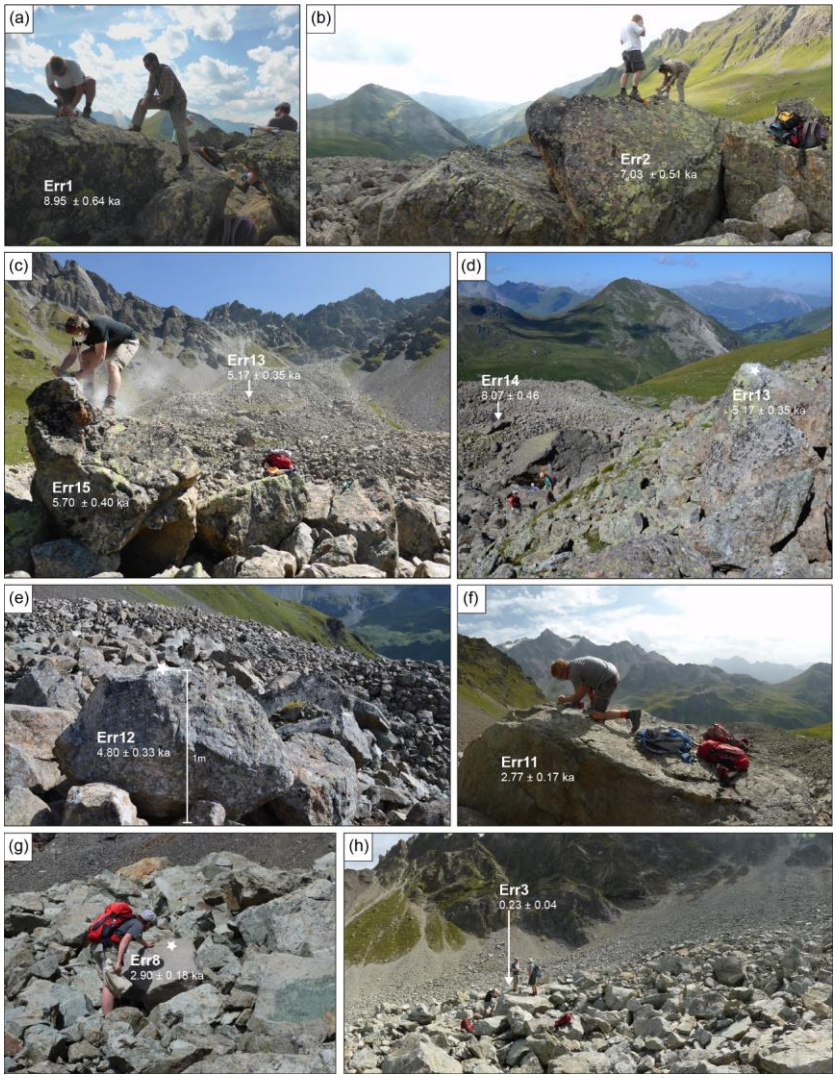

~~The exposure ages in general anticorrelate with elevation and correlate with down-flow distance (Fig. 6). A linear regression between exposure age and distance from the rock glacier root is fitted to the samples on the presently active, high-elevation lobes (units IV–V). As all boulders were sourced in the root zone, the inverse slope can be interpreted as a mean transport rate (cf. Denn~~

Formatiert: Beschriftung

~~et al., 2017), yielding a plausible long-term surface speed of $v_s \approx 30$ cm a^{-1}. The time-axis intercept (Fig. 6) coincides with the transition to the talus. The boulders remained exposed at the surface and were passively transported at the rock glacier surface between talus and top of front slope (Frauenfelder et al., 2005; Scapozza et al., 2014; Winkler and Lambiel, 2018). We conclude that the exposure ages on the active lobe have negligible systematic errors and no overall age shift from inheritance/pre-exposure (systematically "too old") or nuclide loss/incomplete exposure (systematically "too young"). This implies that the transit time in the talus is not recorded by the exposure ages, possibly because it is shorter than the analytical uncertainty and the time "lost" due to snow shielding (not more than decades), or because the boulders were covered in the talus and surfaced only on the rock glacier.~~

Figure 6: Field photographs of selected sampled boulders that are discussed in the text. In panels (d, e, g), the star marks the sampled surface.

~~An exception is the ^{36}Cl age (Err8) that is roughly 2 ka older compared to its neighbouring ^{10}Be ages (Fig. 4). As shielding by snow would make the age even older, the simplest explanation is that Err8 was pre-exposed in the rock wall prior to falling onto the talus and incorporation into the rock glacier. This age is an outlier and is not discussed further.~~

~~On the lower, transitional-inactive lobes (units I–III), the ^{10}Be ages of Err2 and Err15 are significantly younger than the further up-slope sampled Err14. It is unlikely that this apparent age inversion reflects internal creep, as the laminar flow behaviour of a rock glacier makes mixing impossible and contradicts our finding of linear relationship between exposure age and down-flow distance on the active lobes. Therefore, the exposure-age scatter must be introduced by surface processes in the boulder mantle that affect the nuclide inventory of boulders selectively (e.g. Böhlert et al., 2011a; Heyman et al., 2011). On these transitional-inactive lobes, the boulders might have rotated during settling and inactivation, resulting in too low nuclide concentrations and too young ages for boulders Err2 and Err15 (7.03 ± 0.37 and 5.70 ± 0.30 ka, respectively). We consider the ages of 8.08 ± 0.24 to 8.95 ± 0.47 ka (samples Err14, 1) as more representative for the low-elevation lobes.~~

Table 1: ^{10}Be sample information of the Bleis Marscha rock glacier boulders (Err Granodiorite) with location, sample information, blank corrected AMS ~~^{10}Be sample properties and calculated exposure ages (Err granodiorite).~~ ^{10}Be concentration and calculated exposure age.

Sample name	Latitude	Longitude	Elevation	Sample thickness	Shielding factor[a]	^{10}Be concentration[b]	Exposure age[c] ~~(~~erosion corrected~~)~~
	°N	°E	m a.s.l.	cm	-	10^4 at g^{-1}	a
Err1	46.5719	9.7036	244~~8.78~~	1.5	0.9739	23.584 ± 1.216	8948 ± 466 (636)
Err2	46.~~5722~~ 5723	9.~~7052~~7053	248~~1.52~~	1.5	0.9751	18.992 ± 1.004	7027 ± 374 (505)
Err15	46.~~5726~~5727	9.7057	~~2485~~2483~~.3~~	1.0	0.9582	15.257 ± 0.771	5697 ± 290 (399)
Err14	46.5730	9.7070	2498~~.3~~	2.0	0.9484	21.366 ± 0.638	8076 ± 243 (460)
Err13	46.5734	9.7081	2529~~.3~~	2.0	0.9502	14.027 ± 0.659	5169 ± 244 (349)
Err12	46.5737	9.7093	255~~1.72~~	1.5	0.9476	13.234 ± 0.654	4796 ± 238 (332)
Err11	46.5738	9.7102	258~~4.93~~	1.5	0.9450	7.819 ± 0.277	2774 ± 99 (166)
Err10	46.5737	9.7110	261~~1.72~~	1.5	0.9211	3.308 ± 0.425	1181 ± 152 (162)
Err7	46.~~5741~~ 5740	9.7113	2623~~.2~~	1.5	0.9365	1.854 ± 0.161	646 ± 56 (64)
Err6	46.5738	9.~~7121~~7120	2644~~3.1~~	2.0	0.9406	0.860 ± 0.183	295 ± 63 (64)

Err9	46.5742	9.~~7123~~7124	26~~47.8~~50	1.5	0.9204	2.083 ± 0.213	727 ± 74 (82)
Err5	46.5735	9.~~7123~~7122	264~~8.9~~7	1.5	0.9428	2.940 ± 0.202	1001 ± 69 (84)
Err4	46.5735	9.~~7128~~7127	266~~7.5~~5	2.0	0.9392	1.642 ± 0.154	556 ± 52 (59)
Err3	46.5733	9.~~7134~~7133	26~~79.8~~80	1.8	0.9259	0.673 ± 0.115	229 ± 39 (41)

a Shielding correction includes the topographic shielding due to surrounding landscape and the dip of the sampled surface.

b AMS measurement errors are at 1σ level and include the AMS analytical uncertainties and the error of the subtracted blank. Measured ratios were measured against the in-house standard S2007N which is calibrated to ~~the~~ 07KNSTD ~~standard~~.

c Exposure age errors are internal errors (uncertainties represent 1σ confidence range comprising AMS counting errors and errors based on the normalization to blanks and standards). External errors are given in parentheses. Erosion correction for a surface erosion rate of 1 mm kyr^{-1}.

Table 2: ^{36}Cl sample information of the Bleis Marscha rock glacier boulder (Haupt Dolomite) with location, sample information, blank corrected AMS ^{36}Cl concentration and calculated exposure age. ~~^{36}Cl sample properties and calculated exposure age (dolomite).~~

Sample name	Latitude	Longitude	Elevation	Sample thickness	Shielding factor[a]	Cl in rock	^{36}Cl concentration[a,b]	Exposure age[c] (erosion corrected)
	°N	°E	m a.s.l.	cm	-	ppm	10^6 at g^{-1}	a
Err8	46.5741	9.7120	264~~2.6~~3	1.5	0.937	49.63 ± 0.09	0.313 ± 0.014	2890 ± 130 (181)

a Concentration measured against ^{36}Cl/Cl standard K382/4N (Christl et al., 2013; Vockenhuber et al., 2019).

b Sample ratio corrected for laboratory blank of (2.5 ± 0.4) × 10^{-15} ^{36}Cl/^{35}Cl.

c Production rates as in Alfimov and Ivy-Ochs (2009) and references therein. Erosion correction for a surface erosion rate of 5 mm kyr^{-1} (karst weathering/corrosion).

Table 3: Elemental composition of the dolomite sample Err8.

SiO_2	Al_2O_3	Fe_2O_3	MnO	MgO	CaO	Na_2O	K_2O	TiO_2	P_2O_5	LoI	Sm	Gd	Th	U
%	%	%	%	%	%	%	%	%	%	%	ppm	ppm	ppm	ppm
0.45	0.35	0.26	0.06	20.39	31.88	0.06	0.10	0.01	0.01	46.12	0.20	0.10	0.20	6.70

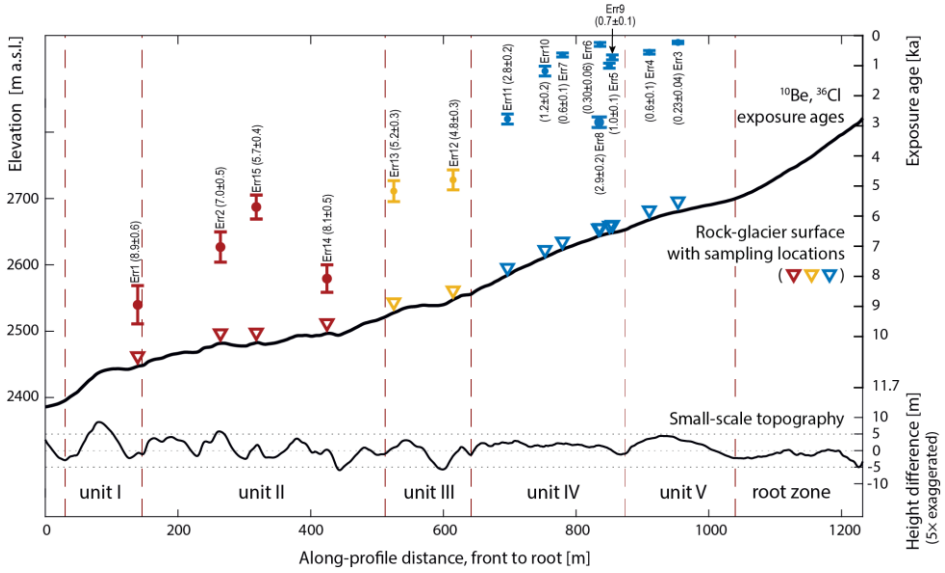

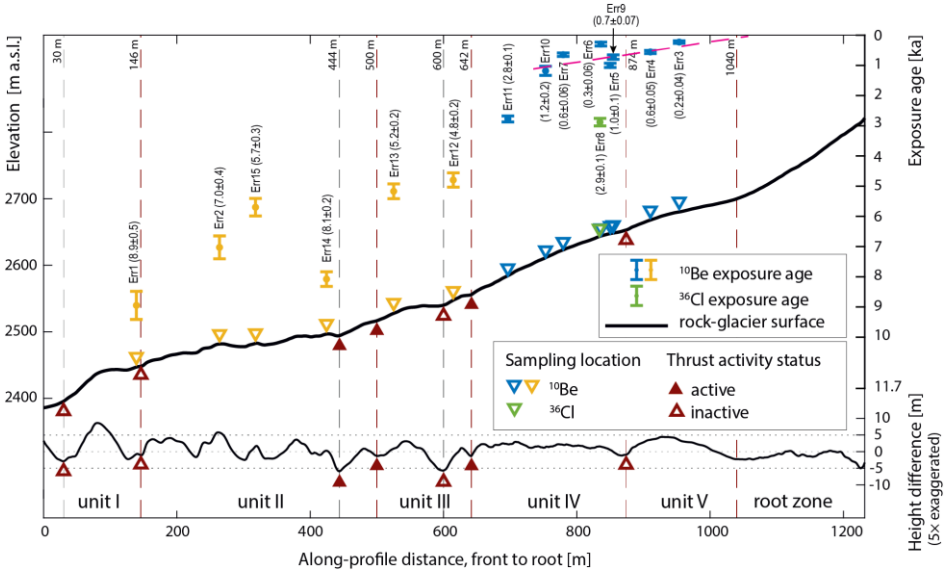

Figure 7: Longitudinal section of ~~rock glacier~~rock glacier surface along the profile line shown in Fig. 4, showing exposure ages, sample location (triangles), surface elevation, ~~and~~ small-scale topography, and morphological units (red dashed lines) ~~(trace shown in Figs. 4, 6)~~. Note the "stratigraphically" directed time axis to emphasize the general anti-correlation of the exposure ages with altitude. Exposure ages and sampling location are projected perpendicular onto the longitudinal profile, not along (unknown) surface isochrons. ~~Linear regression (pink dashed line) of ^{10}Be samples Err3–7, 9, 10, that lie along the central flow line, yield $= -3.28x + 3448$, $= 0.43$, whereas x represents the down-profile distance. This regression line yields $= 0$ a at $x = 1050$ m, coinciding with talus–rock glacier transition. This suggests that pre-travel nuclide concentrations are negligible.~~ The small-scale topography is a high-pass filtered topography computed by subtracting a 100 m running mean from the altitude at each point. ~~Active thrusts coincide with sharp velocity gradients (cf. Fig. 7); this differential movement results in overriding lobes. Inactive thrusts are inner scarps without pronounced velocity changes.~~

4.3 ~~2003/2012~~Modern surface creep rates

Two orthophotos from late summer 2003 and 2012 are matched. The result is a noise-filtered horizontal surface ~~velocity~~ creep rate field ~~and the orientation of the principal strain rate axes~~ for the Bleis Marscha rock glacier and its immediate surroundings (Fig~~s~~. ~~7a, b~~8). ~~Typical~~ Surface ~~speeds~~ creep rates are in the range $v_s \approx$ ~~30~~25–60 cm a^{-1}~~, with peak speeds up to 60 cm a^{-1}~~. There are ~~a few~~ data gaps where the image correlation failed due to decorrelation (non-translational movement, toppling, or vegetation), or ~~missing~~ inadequate input data images (textureless snow fields). ~~The median or modal velocity of the non-moving, stable valley floor is a robust estimate for the magnitude of pre-processing errors (Fig. 8a).~~ Since considerable presumably stable adjacent off-rock glacier areas show apparent surface movements of up to 15 cm a^{-1}, we adopt this conservative value as the significance level. Areas with speeds lower than this level of detection are classified as

non-moving (dark grey areas in Fig. 8).~~The significance level is 5.3 cm a^{-1}, i.e. speeds lower than this threshold are statistically non-significant and respective areas are classified as non-moving (pink areas in Fig. 7).~~

The lowermost unit I is mostly below the level of detection and considered close to immobile. Surface creep rates increase gradually upslope to 25 cm a^{-1} on unit II, while the creep pattern changes: From slow deformation of a central, narrow stripe with outwards gradually decreasing creep rates to a laterally sharply confined, lobe-wide en bloc movement. On units II–IV, surface creep rates increase more stepwise up to 60 cm a^{-1} until the mid-section of unit IV, along with the average surface slope (Fig. 10b). The 'steps' or decorrelation gaps in surface speed coincide with terrain steps that delimit the lobes laterally and frontally. This suggests differential movement of the lobes that override each other, agreeing with field observations of boulder toppling at the over-steepened, 'active' terrain steps (Fig. 4). Important discontinuities are in front of unit III (Fig. 5b) and unit IV (cf. Figs. 7, 10b). Towards the talus, surface creep rates decrease. The orographic left side of the root zone, where unit V is, is more active.

~~The kinematic data suggests the following subdivision of the Bleis Marscha rock glacier in four kinematic domains (front to root, boundaries along isotachs; cf. slope-velocity plot Fig. 8b for the elevation bands and the longitudinal velocity profile in Fig. 9b):~~

~~• *Transitional inactive front*, v_s < 20 cm a^{-1} (elevation band 2400–2475 m a.s.l., units I–II lower part): The lowermost part is characterized by an irregular, "patchy" flow field both in terms of direction and magnitude at an overall low speed. Dominant strain type (shortening ~ compressional stress, stretching ~ extensional stress, slippage ~ shear stress) as well as the effective strain rate varies according to the small-scale topography, and the principal directions are not aligned with the general WSW–NNO rock glacier orientation.~~

~~• *Transition zone*, 20 cm a^{-1} < v_s < 40 cm a^{-1} (2475–2550 m a.s.l.; unit II upper part–unit III): In this part bounded by the 20 cm a^{-1} isotach, a laterally clearly confined surface velocity field emerges. It is smooth with no sharp gradients except along the lateral margins. The speed gradually increases upslope to 40 cm a^{-1}, and the creep direction follows the large-scale topography. The strain is concentrated at the lateral margins, implying that the rock glacier body creeps en bloc. At the margins, the principal axes are rotated by roughly 45° with respect to the general creep direction, typical for simple shear.~~

~~• *Rapid lobe*, 40 cm a^{-1} < v_s < 65 cm a^{-1} (2550–2650 m a.s.l.; frontal/lower part of unit IV): The lower boundary is marked by a stark speed increase (Δv_s = 10 cm a^{-1}, data gap) and a prominent internal front scarp. Above an elevation of 2600 m a.s.l., the velocity decreases again. The velocity field remains smooth and aligned with the large-scale surface slope. Apart from the continuing lateral strain concentration, the deformation is characterized by strong compressive overriding of the lobes in their frontal part and extensional flow behind. The principal axes are aligned with the general creep direction. The shortening is associated with speed decrease (in creep direction) or decelerating creep; stretching/elongation is associated with speed increase or accelerating creep.~~

~~• *Uppermost lobes*, 10 cm a^{-1} < v_s < 35 cm a^{-1} (2650–2760 m a.s.l.; unit V and neighbouring upper part of unit IV): This lobe is individuated based on the slope-velocity relation (Fig. 8b) with a latero-frontal boundary following the morphology. The defining character is the strongly fluctuating surface velocity that becomes gradually decoupled from the smoothed surface slope towards the talus. Strain rates appear random due to the velocity data gaps and decorrelation, likely due to independent, non-translational movement of single boulders. The boundary between root zone and talus is poorly constrained.~~

~~The velocity histogram (Fig. 8a) suggests that the discrimination of the Bleis Marscha activity status into low-elevation inactive versus high-elevation active lobes is at the 20 cm a^{-1} isotach at an elevation of 2475 m a.s.l., implying that (morphological) inactivity is not equivalent to (kinematic) immobility.~~ Data points from the entire rock glacier surface drawn in a slope ~~angle~~ surface ~~velocity~~ creep rate scatter plot (average slope within 100 m radius, Fig. ~~8~~9~~b~~, grey dots) are clustered in a wedge-shaped domain; the few outliers are due to non-translational movement (e.g. sliding, tumbling) and not due to large-area cohesive creep. Higher ~~velocities~~ creep rates are reached at higher surface slope angles, in accordance with the concept of shear-stress driven creep. A clearer slope-velocity relation emerges when data from a 20 m wide stripe along the central profile are highlighted (Fig. 8), because they are unaffected by boundary effects such as lateral drag and non-translational movements. The clear correlation between creep rate and average surface slope suggests that surface creep rates on units II–IV (altitude bands 2475-2653 m asl.) are controlled by topography (via average surface slope) rather than by material property (e.g. effective viscosity). The correlation is lost on the lowermost frontal area (lowermost ~100 m, unit I), where incipient stabilization and possibly loss of ice hampers viscous creep, and on the uppermost unit V, possibly because slope-independent deformation processes other than creep are dominant (cf. Fig. 10b). We explore the relation between surface creep rate, topography and material properties numerically in the next chapter. ~~The maximum slope angle slightly decreases with increasing velocity. Possibly, steep slopes at high deformation rates cannot be sustained by the viscous debris-ice mixture over long time periods but are smoothed out by diffusion. The slope-velocity correlation is clearer when only a 20 m wide stripe along the central profile is considered, unaffected by boundary effects such as lateral drag and non-translational movements. The above defined kinematic domains have their distinct pattern. (i) The velocity of the lowermost, transitional inactive part is low and independent of the 100 m averaged slope (yellow dots). (ii) The 'transition zone' (green) and 'rapid lobe' (dark blue) show a clear correlation between average surface slope and velocity and therefore a strong large-scale topographic control on horizontal surface velocity, in agreement with our understanding of viscous creep. (iii) The correlation breaks down at the uppermost lobe towards the talus (light blue).~~

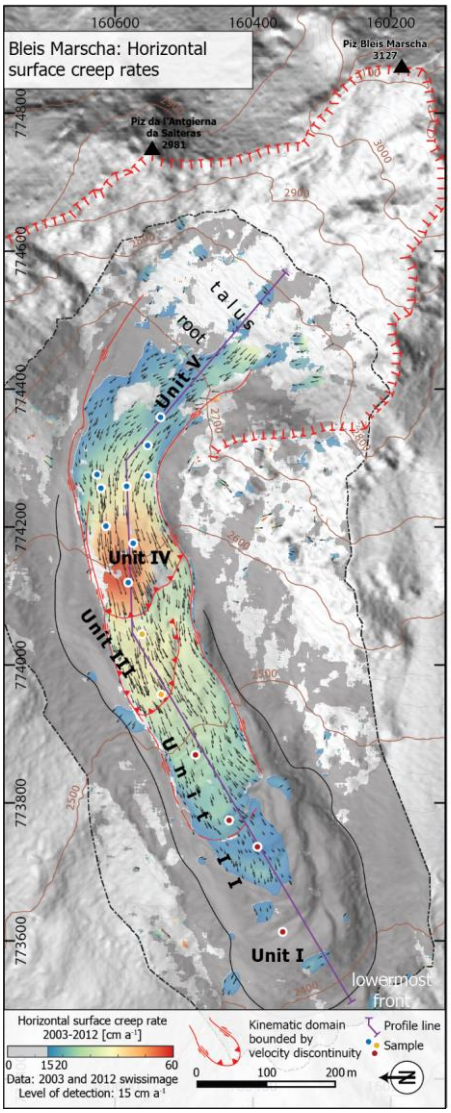
Bleis Marscha: Horizontal surface creep rates
160600
160400
160200
Piz Bleis Marscha 3127
Piz dal l'Antgierna da Salteras 2981
talus
root
Unit V
Unit IV
Unit III
Unit II
Unit I
lowermost front
Horizontal surface creep rate 2003-2012 [cm a-1]
0 15 20 60
Data: 2003 and 2012 swissimage
Level of detection: 15 cm a-1
Kinematic domain bounded by velocity discontinuity
Profile line
Sample
0 100 200 m

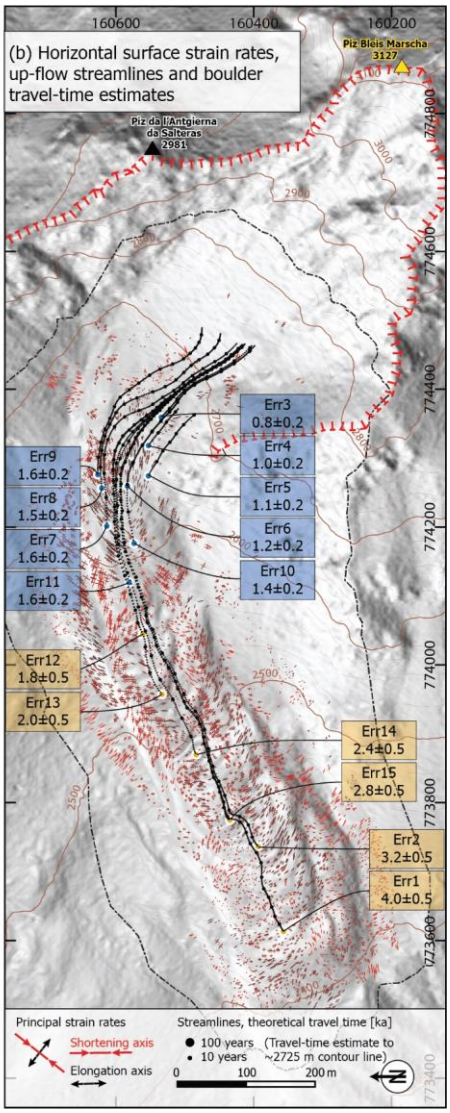
(b) Horizontal surface strain rates, up-flow streamlines and boulder travel-time estimates
160600
160400
160200
Piz Bleis Marscha 3127
Piz dal l'Antgierna da Salteras 2981
Err3 0.8±0.2
Err4 1.0±0.2
Err5 1.1±0.2
Err6 1.2±0.2
Err10 1.4±0.2
Err9 1.6±0.2
Err8 1.5±0.2
Err7 1.6±0.2
Err11 1.6±0.2
Err12 1.8±0.5
Err13 2.0±0.5
Err14 2.4±0.5
Err15 2.8±0.5
Err2 3.2±0.5
Err1 4.0±0.5
Principal strain rates
Shortening axis
Elongation axis
Streamlines, theoretical travel time [ka]
100 years
10 years
(Travel-time estimate to ~2725 m contour line)
0 100 200 m

Figure 8: ~~(a) Plan view of kinematic domains separated by discontinuities such as decorrelation gaps and velocity jumps (cf. Fig. 4 for morphological domains~~Modern horizontal surface creep rates)~~. The noise-filtered horizontal surface velocity field of the Bleis Marscha rock glacier is~~ **derived from two orthophotos from 2003 and 2012.** Level of detection is 15 cm a^{-1}. ~~Kinematic domains are labelled (cf. Fig. 9b). Significance level is 5 cm a^{-1}.~~ **The long temporal baseline of nine years averages inter-annual variabilities in rock glacier creep rates, and is a robust estimate of** modern~~present day~~**, short-term surface kinematics. Morphological** (cf. Fig. 4) **and kinematic discontinuities** (decorrelation gaps and "jumps" in creep rates) largely ~~largely~~ **coincide.** Areas below the level of detection are considered immobile except for the lowermost front (unit I), where a fresh frontal boulder apron and comparison with the 1988 orthophoto indicates slow surface movement (5–10 cm a^{-1}). ~~(b) Horizontal principal strain rates, computed with a spacing of 100 m (finite differences), show the direction of maximum shortening and elongation. The principle axes of strain rate and stress coincide. Up-flow streamlines from the sampled boulders to the ~2725 m contour line give a theoretical trajectory and travel time estimate. Uncertainties of the estimated travel time Δ are estimated as 200 years for the active high-elevation lobes~~

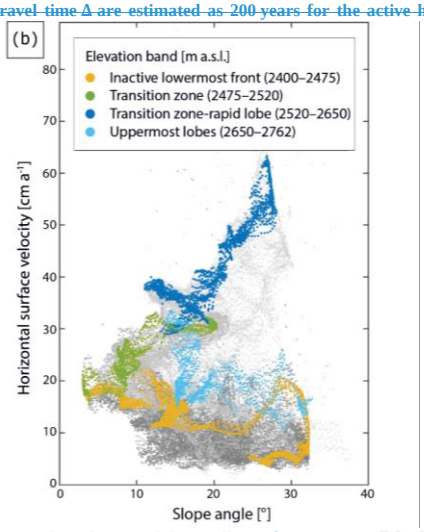

~~(blue rectangles) and 500 years for the transitional-inactive low-elevation lobes (yellow, cf. Fig. 10).~~ **(Hillshade background map reproduced with the authorization of the Swiss Federal Office of Topography swisstopo).**

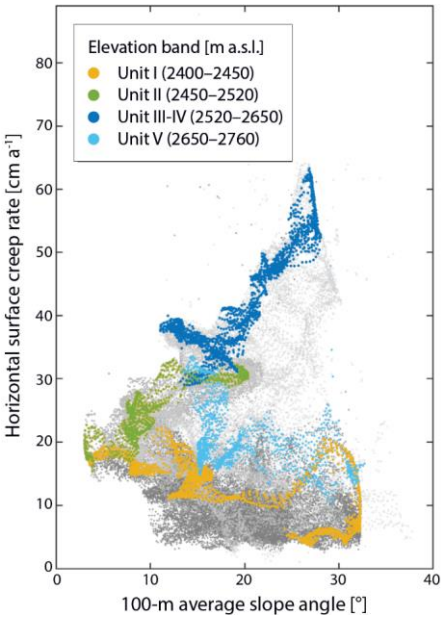

Figure 9: ~~(a) Velocity histogram: The histogram shows the relative occurrence frequency of surface velocities in the reference area (green) and on the Bleis Marscha rock glacier (dark grey). The rock glacier is further subdivided based along the 20 cm a^{-1} isotach in a lower transitional-inactive part (yellow) and an upper active part (blue). (b)~~ Slope–~~velocity~~ creep rate relation: Scatter plot showing the correlation between the 100 m averaged slope (from smoothed ~~DTM~~DEM) and the horizontal surface ~~velocity~~ creep rate for different ~~kinematic domains~~elevation bands of the Bleis Marscha rock glacier. The grey dots are data points ~~on~~ from the entire rock glacier (~~lower part in dark grey/inactive <20 cm a^{-1}~~lowermost part <2450 m asl. in dark grey~~, upper active part in light grey~~ lobes >2450 m asl. in light grey). ~~In color are the data~~ Data points restricted to ~~on~~ a 20 m stripe along the central profile, where the effect of lateral drag is minimal, are colored. The good correlation between surface slope and surface creep rates suggests that on units II–IV, topographically controlled creep is the dominant deformation mechanism.

4.4 Controls on modern surface creep rates~~Semi-qualitative ground-ice content estimates from mechanical modelling~~

For a given rock glacier thickness, layering, and density, the effective viscosity distribution is fitted to the 2003/2012 surface ~~velocity field~~creep rates. We obtain a simplified, but plausible ~~rock glacier~~rock glacier structure (Fig. ~~9a~~10a) that reproduces the ~~velocity~~ image-correlation data within their uncertainty (Fig. ~~9b~~10b). The result suggests that the viscosity in the more slowly moving, apparently ~~transitional~~ inactive low-elevation lobes are only slightly higher than in the active, more rapidly moving high-elevation lobes (Fig. ~~9a~~10a), i.e. that surface creep rates on units II–IV can be explained by topographical parameters (thickness, surface slope) alone. In contrast, the external parts of unit I move more slowly than potentially possible given the comparable surface slope and thickness as unit II. This modelling result corroborates our hypothesis of

topographically-controlled creep on units II–IV and incipient degradation of unit I. ~~The model fails to reproduce the observed velocity jumps between individual lobes (profile at 420 and 620 m) and the differential movement of lobes (Fig. 9b). Vertical profiles of the modelled horizontal displacement ("virtual boreholes") mimic borehole inclinometer measurements of other rock glaciers (Arenson et al., 2002) (Fig. 9a, insets). No boreholes have been drilled on Bleis Marscha rock glacier.~~

~~Rock glaciers are composed of a mixture of debris and ice, each material with a very different mechanical behaviour. However, the continuum approximation averages material parameters in space. Non-viscous processes and interactions between constituents are neglected. Temperature-dependent viscosity, the effect of liquid water, processes at the debris-ice interfaces or grain-to-grain frictional contacts are not captured with the chosen isothermal linear-viscous rheology (Arenson et al., 2002; Moore, 2014; Frehner et al., 2015). Instead, we aim for a rough estimate of multi-annual, largely unchanging material properties. Short-term (daily to seasonal) processes like oscillating temperature or highly variable water flow leading to seasonal deformation variations are neither captured by the numerical model nor expressed in the 9-year averaged surface velocity data set. The effective viscosity is a scale-dependent, homogenized, effective material parameter valid for the bulk material on a decametre-multiyear scale. The only deformation-relevant parameter that hardly changes over a decade must be related to ground ice content because of the high thermal inertia of the ice-rich body. We can therefore treat the inferred effective viscosity as a proxy for ground ice content. Since we have no data on Bleis Marscha subsurface ice content with which we could calibrate the inferred viscosity, we cannot give absolute estimates. Instead, we use the modelling findings to compare the inferred relative ice content in different rock glacier parts.~~

We used the FE code presented in Frehner et al. (2015). The aspects discussed therein (incompressibility, boundary effects) apply analogously in this study. Our synthetic vertical deformation profiles ("virtual boreholes", Fig. 10a, insets) resemble measured borehole deformation profiles from other rock glaciers (Arenson et al., 2002). No boreholes have been drilled on Bleis Marscha rock glacier. Although the simple Newtonian continuum model with vertical viscosity layering does not accurately reproduce deformation mechanisms at the micro scale, it does capture the essential deformation effects that lead to the observed surface creep rates.~~To describe rock glacier creep mathematically, complex rheological constitutive relationships such as viscous power-law relationships have commonly been adopted. However, the roughly parabolic shape of horizontal deformation profiles as measured in several boreholes (Arenson et al., 2002) suggests that the deformation above the shear zone is well represented by a Newtonian flow law (Frehner et al., 2015). In fact, our synthetic vertical deformation profiles ("virtual boreholes" in Fig. 9a, insets) resemble deformation measurements measured on other rock glaciers. The simple Newtonian model with vertical viscosity layering (low-viscosity basal layer) emulates more complex, non-linear deformation mechanisms as observed in rock glaciers.~~

~~The inferred rock glacier structure differs from the (unknown) true structure because of (i) non-uniqueness/ambiguity and (ii) error propagation (Snieder and Trampert, 1999). First, non-uniqueness means that (possibly infinitely) many models explain the data equally well, even though the forward operator (Stokes flow) is unique. There is a fundamental ambiguity attached to the physical forward problem formulation. For example,~~ The solution to Eq. (1) is non-unique, inasmuch as higher surface speed can ~~equally well~~ be achieved with ~~either~~ any combination of greater thickness, steeper surface slope, or

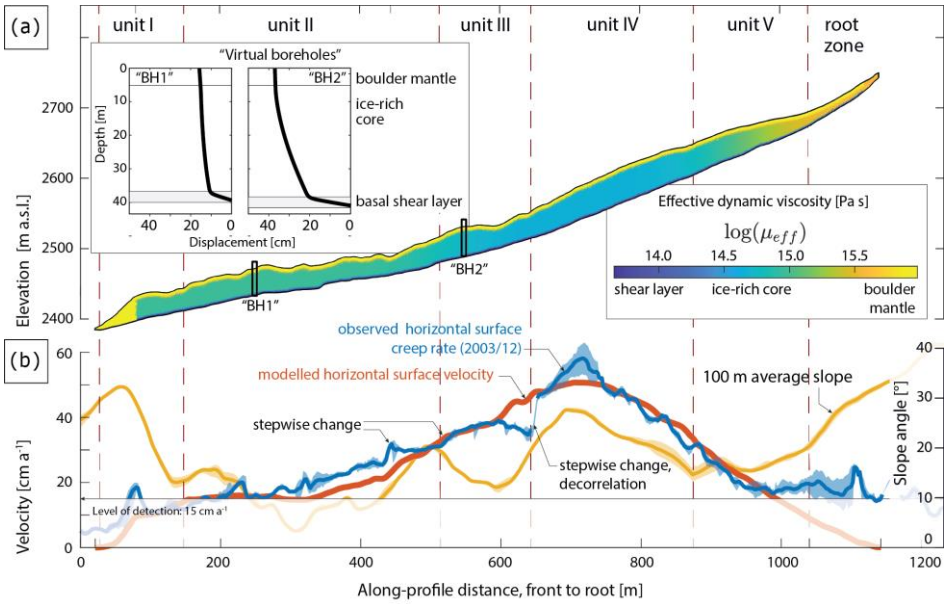

lower viscosity. Large errors in the topographical parameters would undermine the goal of separating topographical from material controls. However, the driving stress and ultimately the deformation is largely governed by the well-constrained average surface slope (not by the basal slope (Nye, 1952)) and the reasonably assessable ~~rock glacier~~rock glacier thickness and density. ~~This is corroborated by the good correlation between surface velocity and averaged surface slope in the sections where viscous creep dominates (Fig. 9b).~~ The remaining unknown viscosity can be estimated ~~within an acceptable uncertainty~~with sufficient accuracy. ~~Second, both the observed data and the forward operator are contaminated with errors that are carried into the estimated model. The inferred structure is drawn towards a rock glacier state for the years 2003/2012 because the model is fitted to data from this measurement period. Due to the long 9 year baseline, an unusual behaviour of a single year is not carried into the model (e.g. the warm summer 2003 with exceptionally high creep rates (Delaloye et al., 2010)).~~

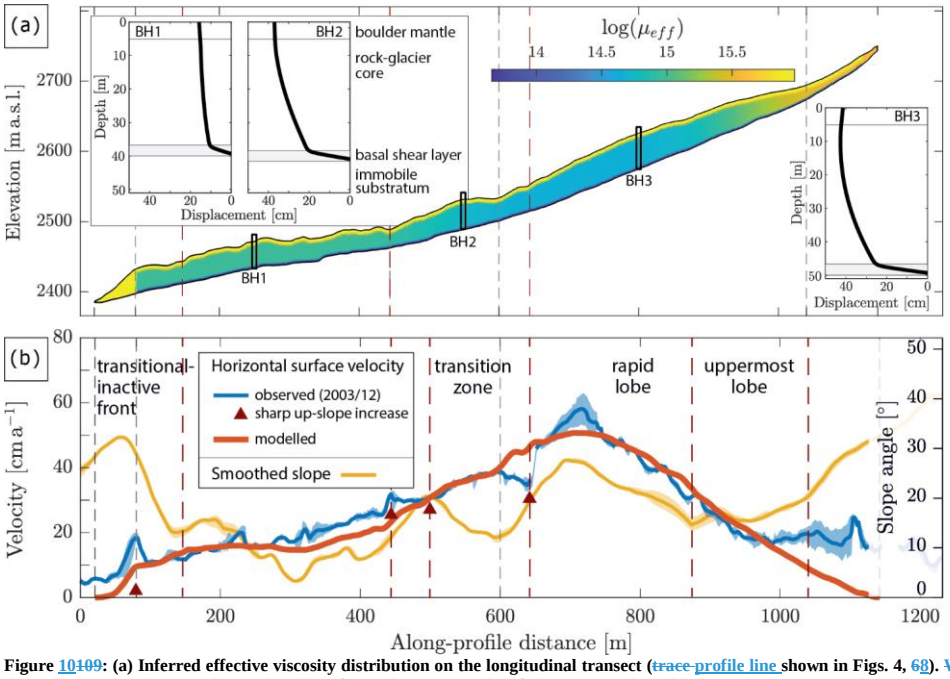

Figure 10~~09~~: (a) Inferred effective viscosity distribution on the longitudinal transect (~~trace~~ profile line shown in Figs. 4, 6~~8~~). ~~With this viscosity distribution, the predicted surface velocity (Fig. 9b) of this estimated model, , match the measured one within the data uncertainty: is one solution to the inverse problem.~~ The inferred effective dynamic viscosity does not vary significantly over units II–IV. Along-profile variations in surface creep rates are primarily controlled by the surface slope. Insets: Modelled yearly horizontal displacements in "virtual boreholes". The strain ~~localisation~~ localization near the base despite the linear stress–strain rate relationship arises from the ~~rock-glacier~~rock glacier ~~parameterisation~~ parameterization with the three-part mechanical layering (boulder mantle, core, basal shear layer). The simple Newtonian model with depth-varying viscosity generates synthetic velocity profiles that resemble borehole deformations measured on other rock glaciers. (b) Longitudinal section of observed surface creep rate (blue line), modelled/synthetic (orange) horizontal surface velocity and the 100 m filtered slope (yellow). ~~Surface~~ Horizontal surface ~~velocity~~ creep rate ~~on of~~ sections dominated by viscous creep roughly ~~closely~~ follow the average surface slope (units II–IV). Correlation is lost ~~at~~ on the ~~stabilised~~ lowermost front and ~~in the~~ talus. ~~Kinematic domains~~The morphologically-defined units I–II, unit III, and units IV–V are ~~delimited~~ separated by sharp speed gradients ('kinematic discontinuities', dark red triangles, cf. Fig. 6~~10~~).

5 Discussion~~: Bleis Marscha landform history~~

By examining the exposure ages and considering the image correlation results we decipher the history of the Bleis Marscha rock glacier over the past 9 ka and put in into the framework of~~. As~~ the ~~regional climate history is reasonably~~ known regional climate history (~~Frauenfelder et al., 2001, 2005;~~ Ivy-Ochs et al., 2009; Böhlert et al., 2011a~~),).we attempt to disentangle~~

~~internal thermo-mechanical/topographic feedbacks from external forcing such as climatic conditions, debris supply and interactions with glaciers.~~

~~The morphologic and kinematic domains coincide and separate the Bleis Marscha rock glacier into two zones of different age and activity status (Figs. 4, 7). Steep scarps outlining the lobes are expressed in the kinematic data as velocity jumps, data gaps and decorrelated areas. The active high-elevation lobes (2550–2700 m a.s.l.) with surface speeds up to 60 cm a^{-1} display clustered exposure ages within 0.23 ± 0.04 to 2.8 ± 0.1 ka. The morphologically transitional-inactive low-elevation lobes (2400–2550 m a.s.l.) show surface speeds below 40 cm a^{-1} and strongly dispersed exposure ages ranging from 4.8 ± 0.2 to 8.9 ± 0.5 ka.~~

5.1 Exposure dating an active rock glacier

Cosmogenic nuclide ages include all of the time that a rock surface is exposed to cosmic rays. However, in nearly all previous studies, the age sought encompasses only the nuclides produced since the boulder has reached its final position (e.g. in a moraine or landslide deposit). Unlike single-age landforms that for the most part formed in short-lived events, active rock glaciers are continually moving and grow over centuries–millennia. Rock surfaces are exposed to cosmic rays in various stages of the landform evolution.

Rock glaciers form on an inclined slope (e.g. talus) when an accumulation with favourable debris-ice proportions reach a critical thickness (cf. Kirkbride and Brazier, 1995; Haeberli et al., 2003, 2006). Viscous creep emerges as the dominant deformation mechanism and the mobilized material begins to creep down-slope under its own weight. Coarse blocks on the rock glacier surface, that form the boulder mantle, are sourced in the rock glacier root and carried towards the front. Conceptually, boulder residence time on the rock glacier surface is the time since initial deposition in the rock glacier root and comprises the travel time (creep-induced, passive transportation during active periods) and, for an inactive–relict landform, time since stabilization of the landform (relict period) (Haeberli et al., 1998, 2003). This model predicts a spatially correlated age signal with downstream systematically increasing surface ages. The ‘conveyor belt’-like advance mechanism affects the rock glacier age structure and the relations between surface velocity, length, and age (Kääb et al., 1997; Kääb and Reichmuth, 2005). Due to the decrease of horizontal speeds with depth and the frontal volume loss mainly from excess ice meltout, the rock glacier surface moves faster than the advancing landform itself (Haeberli et al., 1998; Frauenfelder et al., 2005; Kääb and Reichmuth, 2005). Surface exposure ages atop the front of rock glaciers give the lower bound of the landform age (cf. Scapozza et al., 2014; Winkler and Lambiel, 2018).

On an active rock glacier, the cosmogenic nuclide concentration adds up all of the following periods of exposure (Table 4):

1. Pre-exposure in the headwall (bedrock inheritance),
2. Transit time in the talus or during intermediate storage upstream in the talus,
3. Transport on the moving (active) rock glacier (travel time),
4. Sitting at the (quasi-)stabilized position (inactive rock glacier or relict rock glacier deposit).

Formatiert: Listenabsatz, Zeilenabstand: Mehrere 1.15 ze, Nummerierte Liste + Ebene: 1 + Nummerierungsformatvorlage: 1, 2, 3, … + Beginnen bei: 1 + Ausrichtung: Links + Ausgerichtet an: 0.63 cm + Einzug bei: 1.9 cm

As in other cosmogenic nuclide studies, post-depositional surface processes like boulder surface weathering, spalling, unaccounted for shielding, rotation and toppling lead to a lower total boulder nuclide inventory (Ivy-Ochs et al., 2007; Heyman, 2011).

Table 4: Processes that affect measured cosmogenic nuclide concentration in a boulder on an active rock glacier (see text for discussion). Surface processes like exposure in the bedrock (inheritance), post-depositional weathering, spalling, unaccounted for cover or shielding, rotation and toppling affects single boulders to variable degrees and largely independently from their neighbors.

Process	Effect on nuclide inventory and exposure age
Ideal nuclide buildup '^{10}Be, ^{36}Cl clock' dates the onset of boulder travel in the rock glacier root	Ideal nuclide inventory: travel time and time elapsed since rock glacier stabilization
No inheritance, immediate deposition on rock glacier root with rapid (or buried) transfer in talus, exposure during transport embedded in boulder mantle, fixed boulder orientation, continued exposure after rock glacier advance stops	Complete record of (1) transport on advancing rock glacier, and (2) sitting at (quasi-) stabilized position on inactive rock glacier or relict rock glacier deposit
Pre-depositional effects '^{10}Be, ^{36}Cl clock starts too early'	Inherited nuclides or excess nuclides from previous exposure, 'too old' exposure ages
Exposure in rock wall (bedrock inheritance)	Higher nuclide concentration
Exposure during upstream storage prior to deposition on rock glacier, e.g. in talus or moraine	Higher nuclide concentration
Post-depositional effects 'slowing or resetting the ^{10}Be, ^{36}Cl clock'	Nuclide concentrations lower compared to 'true' exposure time, 'too young' exposure ages
Boulder instability: rotation, toppling or overturning, relocation	Lower nuclide concentration from changing dip and orientation of surface, incomplete exposure (self-shielding) to variable degree
Spalling	Lower nuclide concentration
Surface weathering (erosion)	Lower nuclide concentration (minor effect, correctable)
Cover by snow, ice, vegetation, soil, debris	Lower nuclide concentration (if unaccounted for, partly correctable)

5.2 Interpretation of the Bleis Marscha boulder exposure ages

Our exposure ages in general anticorrelate with elevation and correlate with down-flow distance from the rock glacier root (Figs. 4, 7), conformable to the rock-glacier formation model. Nevertheless, ages from individual lobes show 'geologic scatter'. How do the processes listed in Table 4 apply to the Bleis Marscha rock glacier?

5.2.1 Boulder nuclide inventories on a moving rock glacier

Significant pre-exposure in the cirque headwalls seems unlikely because for talus rock glaciers like Bleis Marscha, fed by scree from the retreating headwall, headwall erosion is rapid (cf. Mohadjer et al., 2020; Steinemann et al., 2020). Back-of-the-envelope estimates of long-term average debris fluxes of the rock glacier lobe IV and V are in the order of 720 (<900) $m^3 a^{-1}$, calculated from mean speeds of 400 m/1200 a (length of lobe divided by exposure age), and a rock glacier width of 120 m (<150 m), a height of 30 m, and a debris fraction of 0.6. These debris fluxes correspond to head-wall erosion rates of ~2.3–2.9 mm a^{-1}. At this accumulation rate meters of talus are built-up at the foot slope in decades to centuries as testified by the abundant fresh talus cones within the footprint of the LIA Bleis Marscha cirque glacier (Fig. 5a). With respect to their ice-cored moraine study, Crump et al. (2017) point out that it may be difficult to detect low levels of ^{10}Be inheritance, but that it becomes unlikely for boulders larger than ca. 1 m side length because of strong self-shielding in the bedrock wall (rapid drop-off of ^{10}Be production with depth). Boulders can also be exposed in the talus or any other reservoir (e.g. moraine deposit) prior to entering the rock glacier system. Comparison of aerial photos over several years shows the rapid accumulation of talus since the LIA (see above), suggesting that nuclide accumulation in a boulder while in the talus or at the talus foot is likely not significant as the scree is quickly covered. Critically, the young exposure ages in unit V (see also below) verify rapid deposition onto the rock glacier. If inheritance from bedrock exposure is unlikely and storage in the talus with exposure at the surface is likely to be brief, then nuclide concentrations should record the time elapsed on the rock glacier surface. This would include travel time and all of the time that a boulder is stable, whether in final relict deposit or when the rock glacier is less active. This suggests that most of the 'geologic scatter' of our data is due to post-depositional processes (Table 4), with instability in boulder position being the prime candidate.

Boulder GPS data reported by Lambiel and Delaloye (2004) demonstrate small (cm), slow, three-dimensional rotational movement of boulders, pointing to slightly variable orientation of the sampled surface and to the possibility of toppling or overturning over longer periods of time. Boulders might roll or slide down steep scarps in front of rock glacier ridges (Kääb and Reichmuth, 2005) or topple into furrows. Ulrich et al. (2021) detected creep-independent, 'gravity-induced boulder movement' over a three week period at the steep (~30°) frontal part of the Äußeres Hochebenkar rock glacier with repeated terrestrial laser scans. Boulder instabilities are likely greater, the faster the rock glacier moves, and exacerbated by changes in surface elevation due to frost heave, thaw settlement, degradation or collapse of the underlying ice-rich core, similar to ice-cored moraines (e.g. Crump et al., 2017), what we however did not observe on Bleis Marscha. Boulders are subangular to subrounded even in the youngest parts of the rock glacier (units IV–V; Fig. 6), evidence that knocking off of boulder corners during movement (jostling) or falling off the front of ridges is occurring. Addition of a boulder to a lobe due to recent rock fall as observed at Murtèl (Upper Engadine) in August 2020 (personal observation), would also yield a too young age. In the case of recent events, fresh boulder appearance calls this out. The effect of (~uniform) boulder surface weathering is accounted for in the age calculation. It is only a few percent and lies within the uncertainties of an individual exposure age. On the other hand, (non-uniform) spalling, e.g. from frost shattering or friction between the boulders, potentially leads to

more severe lowering in nuclide concentration. Recently spalled surfaces, as revealed by their 'fresh' appearance, were not sampled. Unaccounted for shielding also leads to 'too young' exposure ages. The effect of snow cover was likely more pronounced for the smaller, less windswept boulders in the high-elevation lobes (units IV–V) where snow cover lasts longer, but also more uniform over the less rough surface. Strict constraints on how much snow and for how long hinder such a correction whose effect is limited to a few percent.

5.2.2 Three Bleis Marscha rock glacier generations

Formatiert: Deutsch (Schweiz)

In light of the above discussion of the various factors contributing to cosmogenic nuclide concentrations in active rock glacier boulders, we now discuss the specific Bleis Marscha results. The cumulative effect of slight boulder instabilities and small under-exposure from rotation added up over millennia likely plays a role for the 'geologic scatter'. We think that the effect of stochastic boulder instabilities in general exceeds inheritance, although neither can be excluded in individual cases. The Bleis Marscha exposure ages are tendentially skewed towards 'too young'.

The morphologically continuous units I and II are the lower elevation, thus oldest units at Bleis Marscha. The exposure age of unit I is 8.9 ka (Err1, Fig. 6a). Of the three ages from boulders across unit II, two ages Err2 (7.0 ka) and Err15 (5.7 ka) are younger than the further up-slope boulder age Err14 at 8.1 ka (Fig. 6c, d). Boulders Err1 and Err14 are large and flat-lying with basal side lengths >3 m making it more likely that they roughly maintained their orientation as the rock glacier moved. In contrast, boulders Err2 and 15 are cigar-shaped, i.e. prone to rolling, and not very firmly embedded in the boulder mantle (Fig. 6b, c). We consider the ages for the latter two as 'too young'. We suggest that units I–II started forming at ~8.9 ka. Unit III occupies an intermediate topographic position in the Bleis Marsch rock glacier and is separated by a morphological discontinuity from the lower units I–II (Figs. 4, 5b). Two consistent ages Err13 (5.2 ka, Fig. 6d) and Err12 (4.8 ka, (Fig. 6e) also point to a 'time gap' between units I–II and unit III. The partly stabilized and vegetated terrain step immediately downstream of Err13 is the stabilized front of this lobe which we interpret to have formed at ~5.2–4.8 ka. Rock glacier units IV and V comprise the higher elevation more rapidly moving lobe of Bleis Marscha (Fig. 5a). Ages for unit IV range from 2.9 ka to 0.3 ka. The ^{36}Cl age of 2.9 ka for Err8 seems incongruous with its position and the fact that a nearby boulder (Err9) is, at 0.7 ka ^{10}Be age, 2 kyr younger. In comparison to the several dated boulders on unit IV, it is likely that boulder Err8 experienced pre-exposure in the bedrock. Inheritance is plausible given the small dimensions of the sampled boulder (0.7×1.0×1.5 m, Fig. 6g; see discussion above on Crump et al., 2017) and the crucial fact that ^{36}Cl is produced deeper into rock than ^{10}Be (Alfimov and Ivy-Ochs, 2009). This does not greatly affect our interpretation that lobe IV initiated at ~2.8 ka (age of Err11, Fig. 6f). The time gap to unit III coincides with a morphological (frontal terrain step) and kinematic discontinuity (Figs. 4, 8, 10b). Unit V is the highest elevation, youngest unit. It emanates from the footprint of the LIA glacier 100–150 m away from the foot of the talus, to what the two ages of 0.56 ka and 0.23 ka agree well.

We summarize the three interpreted Bleis Marscha formation phases, defined as the period during which the lobe is fed in the root zone (Fig. 11). Our data suggests that the early Holocene generation (units I–II) began forming at ~8.9 ka. The

formation phase lasted at least until ~8.1 ka as indicated by the upstream-most exposure age. Its youngest surface in the root zone has been overridden and buried by subsequent rock glacier generations. At the latest at ~5.2 ka, the minimum formation age of the mid-Holocene generation (unit III), units I–II must have been cut off from their debris source in the cirque. Analogously, the formation phase of the mid-Holocene generation with ages in the range ~5.2–4.8 ka ended at ~2.8 ka the latest, when it was overridden by unit IV and disconnected from the talus. The youngest late Holocene generation (units IV–V) began forming at ~2.8 ka. Coinciding morphological discontinuities (steep terrain steps, Fig. 4), 'time gaps', and kinematic discontinuities (velocity jumps, data gaps; Fig. 8) separate units I–II, III, and IV–V from each other. We interpret that Bleis Marscha is not a continuous 'stream', but a stack of three overriding lobes, each with its own, discrete formation phase.

~~**5.1 Surface kinematics across time scales**~~

~~In order to understand what the exposure ages represent, we compare the measured exposure age with travel time computed from streamlines of the present, short-term (2003/2012) surface velocity field (Fig. 10). Theoretically, boulder residence time on the rock glacier surface is the sum of the travel time (transportation during active period) and time since cessation of advance (transitional inactive period) (Haeberli et al., 1998, 2003). Conceptionally, boulders move along the 1:1 line during active periods where boulder surface residence time equals both exposure time (i.e. ideal, complete exposure) and travel time (i.e. representative velocity field, steady-creep conditions (Haeberli et al., 2003)). There are two main clusters in the travel time exposure age space: (i) Below the line of equal time estimates ("1:1 line") group the high-elevation samples with young exposure ages <1.2 ± 0.2 ka, and (ii) above the 1:1 line the low-elevation samples with older exposure ages.~~

~~< , below 1:1 line (Fig. 10): The exposure ages for the samples located on the presently active upper lobes are slightly less than the travel times by about 10–100 years, which is within the uncertainty margins. The measured surface velocity field is representative, and the discrepancy is smaller the closer the samples are to the central flow line (Err3, 4, 5, 10), where the influence of lateral viscous drag is smallest.~~

~~The exposure ages from the active lobe suggest a long-term averaged surface velocity of not more than 30 cm a^{-1} over the last ~1000 years on the uppermost lobes, a value that is surprisingly consistent with the 2003/2012 short-term horizontal surface speeds (moderate v, ~ 30 cm a^{-1}, <65 cm a^{-1}). Topographic gradient, surface velocity and axes of principal strain rates are aligned on a 100 m scale (Fig. 7). Creep direction and magnitude are governed by the average surface slope. The consistency between present velocity field with long-term kinematics (in terms of average surface speed) and present 100 m scale topography (in terms of creep direction, speed, and strain rates) of the upper lobes indicates that the permafrost body is in equilibrium.~~

~~Our data on the active lobe of Bleis Marscha rock glacier show that the exposure ages for an undisturbed rock glacier lobe can be addressed as (minimum) travel times. While travelling during the active phase, boulders remain mutually interlocked within the clast-supported framework and the age dispersion remains small. Notably, it also shows that pre-travel nuclide build-up, inheritance, and pre-exposure in the rock wall or on the talus are insignificant.~~

~~> , above 1:1 line (Fig. 10): The exposure ages for the samples located on the presently transitional-inactive lower rock glacier lobes considerably exceed the travel time by up to several thousand years. Although present-day surface velocity field is likely not representative for their active period, already the morphologically inactive appearance, exposure age inversions, the large age dispersion exceeding analytical uncertainty, and the quotient of rock glacier length (1100 m) to typical surface speed (~30 cm a^{-1}) clearly indicates that the exposure ages (<8.9 ka) are much too old to be addressed as travel time estimates.~~

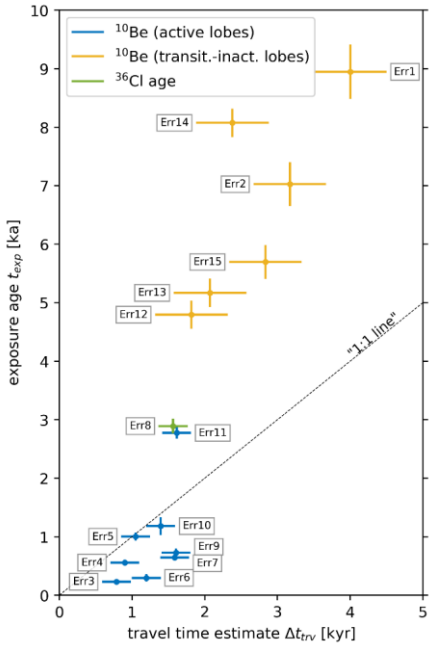

~~Figure 10: Travel time estimate **Δ** versus exposure ages . By comparing the kinematic signal from long-term exposure ages and short-term image correlation results, we construct a framework on how to interpret the exposure ages. Travel time estimate **Δ for each sampled boulder is derived from the image analysis as the travel time between the current boulder position and the 2725 m a.s.l. contour line (Fig. 7b). Uncertainties of the exposure ages are the analytical uncertainties (internal errors). Cf. Fig. 7b for travel time uncertainty estimates. In a hypothetical steady-state case with perfectly representative velocities and ideal exposure ages, the~~

~~**boulders move along the line of equal time estimates ("1:1 line"). This "1:1 line" separates the boulder exposure ages on the active lobes (below) from the ages on the transitional-inactive lobes (above, long inactivity time). The exposure age of Err8 is possibly "too high" because of nuclide inheritance. The travel time estimate of Err11 is likely affected by internal topographic feedbacks (kinematic wave and sudden terrain drop-off, cf. Fig. 5a).**~~

~~The surface deformation pattern on the Bleis Marscha rock glacier changes below an elevation of 2500 m a.s.l. (Fig. 7b). The transitional-inactive, slowly collapsing lower lobes are characterised by an irregular surface velocity field that is strongly coupled to the small-scale topography. Creep direction and magnitude are governed by the local surface slope, i.e. the ridges settle and collapse. Intermittent boulder instability during inactivation has been affecting the nuclide inventory of each boulder individually, leading to incomplete exposure by self-shielding and nuclide loss by weathering or spalling, and ultimately to tendentially underestimated true exposure times ('apparent rejuvenation'). This results in a large dispersion of exposure ages and exposure age inversions on the low-elevation rock-glacier lobes.~~

~~Buckle folding in response to compressive flow of a layered medium likely was the dominant formation mechanism for the transverse furrow-and-ridge micro-topography (cf. Frehner et al., 2015). However, the 2003/2012 strain-rate data do not show along-flow shortening and compression (Fig. 7b). Therefore, the observed micro-topography on the lower rock glacier lobes is an expression of palaeo-stress conditions that are different from the present-day stress field. The morphology memorises the cumulative deformation history over the lifetime of the rock glacier and is largely preserved during inactivation (Frauenfelder and Kääb, 2000).~~

~~The field above the 1:1 line is characteristic for rock-glacier lobes whose activity phase has ceased. A long time has passed since surface advection came to a halt, and the travel time is within the uncertainty of the exposure age. The exposure ages are rather inactivity or stabilisation ages than travel time estimates, as previously reported (Moran et al., 2016; Steinemann et al., 2020).~~

~~We find that exposure ages need to be interpreted according to the dynamic history of the sampled rock-glacier lobe. On undisturbed lobes where the current surface creep is concordant with the micro-topography, exposure ages represent (minimum) travel times. This applies to active lobes without destabilisation. On 'discordant' lobes where micro-topography reflects different stress conditions and must have undergone disruptive dynamic changes, the exposure ages represent time elapsed since the major dynamic change. Inactivation or destabilisation are such disruptive events. With this interpretation scheme for exposure ages on active to relict rock-glacier lobes, we reconstruct the Bleis Marscha rock-glacier development in three major phases, early, middle, and late Holocene (Fig. 11).~~

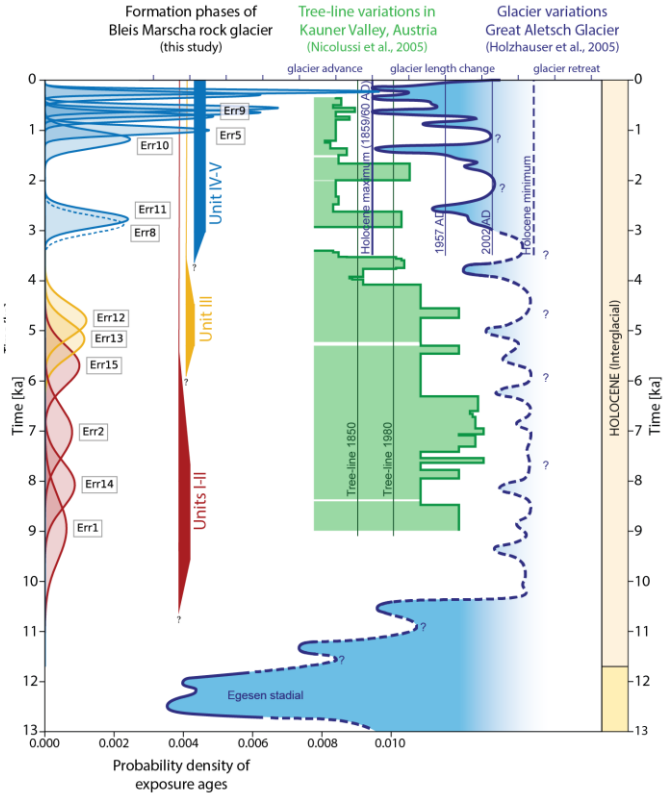

890 **Figure 11: Bleis Marscha ~~rock glacier~~rock glacier ~~activity~~ formation phases in the framework of the general climate evolution in the Central-Eastern Alps during the Younger Dryas and the Holocene (modified from Ivy-Ochs et al. (2009) and Singeisen et al. (2020)). Climate proxies are Great Aletsch glacier length variations (modified from Holzhauser et al., 2005~~)~~) and Kauner valley tree-line variations (Nicolussi et al., 2005) ~~and varve deposition in Lake Silvaplana (Upper Engadine; Leemann and Niessen, 1994)~~.**
895 ~~**The probability densities of the exposure ages show** We interpret **two** three **distinct generations separated by a millennia-long phase of inactivation**~~: Early Holocene (~8.9–8.0 ka, after retreat of the Egesen glaciers of the Younger Dryas cold phase) of low-elevation units I–II, Middle Holocene (~5.2–4.8 ka, after thermal maximum) of unit III, and Late Holocene until present (since ~2.8 ka, roughly coeval with late Holocene cooling and glacier re-advances~~The currently transitional-inactive first generation developed shortly after the Egesen cirque glacier retreat and became inactive in the early Holocene. The disturbance associated with inactivation (settling, boulder weathering and spalling) resulted in nuclide loss and the observed large age dispersion. The**
900 ~~**exposure ages record the (minimum) time elapsed since inactivation. The currently active second generation developed coeval with the late Holocene cooling and glacier re-advances. The precise exposure ages of the last 1.2 ka correlate with distance from the source, suggesting stable permafrost conditions. These undisturbed exposure ages record time elapsed since boulder emergence from the talus and boulder travel tim**~~) of high-elevation units IV–V. The initiation of the three Bleis Marscha generations appear to correlate with Holocene climate oscillations.~~e.~~

905

5.3 Implications

5.3.1 Episodic formation

In the Bleis Marscha cirque, Holocene rock glacier formation occurred in three distinct phases. These appear to be correlated to major Holocene climate shifts. The early Holocene generation (units I–II) is confined within, but not connected to Egesen lateral moraines (Schlosser, 1990). From this crosscutting relationship and the oldest and lowermost (minimum) formation age atop its front of 8.9 ka (Err1), it follows that these lobes must have formed after the Egesen cirque glacier starvation during the late Younger Dryas (Frauenfelder et al., 2001; Kerschner and Ivy-Ochs, 2008; Ivy-Ochs et al., 2009, Ivy-Ochs, 2015). After 10 ka, the climate shifted towards warmer conditions (Schimmelpfennig et al., 2014; Solomina et al., 2015). Already by the middle Holocene, the lower continuous permafrost boundary rose to likely above 2600 m a.s.l. (current -2°C MAAT isotherm, Fig. 3), and the tree line was higher than today (Fig. 11; Nicolussi et al., 2005). The early Holocene debris volume (units I–II) is twice the late Holocene debris volume (units IV–V) that took ~3 kyr to build up. This is a conservative estimate from the corresponding lengths (factor 1100 m/480 m ≈ 2.3) and surfaces areas (factor of ~2.7), assuming similar thickness and debris content, and that units I–II must extend as far up to their source of Err Granodiorite as both younger generations. Given the early Holocene warming and the formation timing of the mid-Holocene generation (~5.2–4.8 ka), it seems unlikely that the formation phase of the early Holocene generation was longer than 6 kyr. This rough comparison of debris supply rates points at a more intense early Holocene debris release compared to the late Holocene average. Possibly, the rapid early Holocene buildup was conditioned by debris from warming-induced rapid head wall weathering (Kenner and Magnusson, 2017; Kenner, 2018). Considering the climate resilience of debris-mantled Bleis Marscha lobes (discussed below), the end of the formation phase seems more likely linked to declining or imbalanced supply of debris and ice in proportions no longer susceptible for rock glacier creep.

The ages of the mid-Holocene unit III suggest a period of enhanced Bleis Marscha rock glacier activity at around 5 ka (~5.2–4.8 ka). Several lines of evidence, including radiocarbon data (Joerin et al., 2006) suggest a dominantly warm interval around that time perhaps punctuated by brief cold snaps (Solomina et al., 2015, 2016; Nicolussi et al., 2005, Kaufmann et al., 2020). Nevertheless, data from Tschingelgletscher (Berner Oberland; Wipf, 2001) and the Miage glacier (Mont Blanc massif, Deline and Orombelli, 2005) point to glacier advances around 5 ka, which is as well documented by the mummification of the Tyrolean Iceman after 5320–5050 cal BP (Kutschera et al., 2017) due to ice coverage which roughly persisted until 1991. Bohleber et al. (2020) point out an elevation dependency on the onset of middle to late Holocene glacier advances, suggesting that at the elevation of Bleis Marscha, the transition to colder conditions may have already begun.

In the late Holocene, after approximately 4 ka, climate cooled, timberline moved to lower elevations, and glacier advances became more frequent, longer and more severe compared to the middle Holocene, culminating in the LIA at ~1350–1850 CE (Fig. 11; Joerin et al., 2006; Ivy-Ochs et al., 2009; Le Roy et al., 2015; Solomina et al., 2016; Badino et al., 2018). Air temperature oscillations and concomitant freeze-thaw cycles weakened the headwall and increased frost shattering and debris

production, enhanced by the tectonically weakened fault zone in the headwall (Figs. 3–5a). Our data suggests that the late Holocene generation began forming roughly coeval with this climatic shift.

According to the dual-threshold model presented in Kirkbride and Brazier (1995), initiation of a new rock glacier lobe occurs when an external climate threshold and an internal talus thickness (shear-stress threshold) are crossed simultaneously. In Bleis Marscha cirque, debris production is high, as shown by the overfilled talus with lots of fresh rock fall since LIA (Fig. 5a). The internal threshold is not a limiting factor, and the Bleis Marscha rock glacier generations seem to reflect more the external climate threshold.

5.3.2 Slow degradation

The creep of the early-mid Holocene generations (units II–III), although with 15–35 cm a^{-1} moving not as fast as the younger unit IV at 40–60 cm a^{-1}, is topographically controlled rather than by the creep susceptibility of the rock glacier body. This is shown by the good slope-creep rate correlation (Fig. 9) and the FE modelling results (Fig. 10). Moreover, cohesive creep and en bloc movement of these entire morphologically delineated lobes with sharp lateral velocity steps (Figs. 4, 7) indicates stress transmission and requires (excess) ice as 'cement' – notably beneath an early–middle Holocene boulder mantle, currently located below the -2°C MAAT isotherm (Fig. 2). Merely the southernmost fringe of the lowermost units I–II shows signs of incipient degradation. For lack of direct data on the interior of Bleis Marscha, the age of the inferred Bleis Marscha ice is not known and can principally be original or later recharged ice (Giardino and Vitek, 1988; Colucci et al., 2019). From the impression of a still intact looking microtopography (Fig. 5b), we think that the ice in units I–II and III is largely as old as its covering debris mantle, thus of early and mid-Holocene age, respectively. Otherwise, if advanced meltout occurred, the surface would look more disrupted and collapsed.

Persistence of ice is characteristic for rock glaciers, owed to the insulating openwork debris mantle (~active layer) and the cooling effect of air circulation (Colucci et al., 2019; Jones et al., 2019; Kellerer-Pirklbauer, 2019). For example, preservation of early Holocene ice through the mid-Holocene warm period is interpreted by Krainer et al. (2015) for the Lazaun rock glacier (South Tyrol). The close connection between surface substrate and ice preservation seems exemplified on Bleis Marscha by the stabilized right-lateral parts of unit III (Figs. 3, 5a), that do not move despite the mechanical load of the rapidly overriding unit IV. The local ground thermal regime beneath the fine-grained surface cover (fractured radiolarite) is less susceptible to permafrost conditions (Harris and Pedersen, 1998; Schneider et al., 2012).

5.3.3 Late Holocene glacier-rock glacier coexistence

During the late Holocene cold phases, the Bleis Marscha cirque was intermittently occupied at the most by a perennial ice patch or a glacieret (Frauenfelder et al, 2005), likely not larger than the LIA extent as mapped in the mid-19th century (Dufour, 1853; Siegfried, 1887). The thin, stagnant cirque glaciers could neither mechanically nor thermally erode the rock glacier; permafrost and the pre-existing rock glacier outlasted beneath the ice patches (Frauenfelder et al., 2001, 2005).

Stable cryotic conditions during the late Holocene are plausible in the high-elevation (>2700 m a.s.l.) cirque floor that is in the continuous permafrost belt even today (Gruber et al., 2006; Boeckli et al., 2012). "Mild" periods apparently were not long and warm enough for permafrost degradation, the more in view of the climate resilience of the debris-mantled ice-rich bodies. The equilibrium line altitude in the steep Bleis Marscha cirque headwalls oscillated in elevation, as likely did relative accumulation rates of ice and debris, with higher relative debris input during ice-free "mild" phases (Anderson et al., 2018; Kenner et al., 2018). Also, the coarse debris transport alternated between glacial transport during cold phases and permafrost creep during glacial "mild" phases (Zasadni, 2005). Despite these oscillating growth conditions in the rock glacier root, the morphologically continuous surface (absent topographic steps) of unit IV with boulder exposure ages ranging from 0.5–2.8 ka suggests undisturbed growth from ~2.8 ka to pre-LIA.

5.2 Early Holocene: Rapid debris-conditioned growth

A set of lateral moraines descending on both trough shoulders of the upper Val d'Err, short moraine segments parallel to the lower lobes of the Bleis Marscha rock glacier (Fig. 3) and hummocky moraines at the valley bottom near Alp d'Err were assigned to the Egesen stadium by Frauenfelder et al. (2001) and suggest that upper Val d'Err was still heavily glacierised during the early Younger Dryas (YD). However, during the late YD, the climate shifted to more continental, dry-cold conditions, and the Egesen glaciers starved (Kerschner and Ivy-Ochs, 2008; Ivy-Ochs et al., 2009, Ivy-Ochs, 2015) (Fig. 11). Palaeoclimatic reconstructions by Frauenfelder et al. (2001) indicate that the lower permafrost boundary was depressed several hundred meters more than the glacier equilibrium line altitude (ELA), opening a wide periglacial altitude belt (cf. Steinemann et al., 2020). This dry-cold permafrost phase lasted from late YD until about 10 ka.

The low-elevation, older-generation part of the rock glacier (units I–III) is confined within, but not connected to Egesen lateral moraines and must have derived its Err granodiorite debris from the previous Egesen Bleis Marscha cirque glacieret accumulation area (in the back of cirque), i.e. the rock glacier must have formed *after* the Egesen cirque glacier starvation (Frauenfelder et al., 2001). From this crosscutting relationship and the oldest and lowermost stabilisation age atop its front of 8.9 ± 0.5 ka (sample Err1) we narrow the emplacement to a short activity period within about 11.5 and 9.0 ka. This rapid, post-YD to earliest Holocene formation agrees with reconstructions in the Julier area by Böhlert et al. (2011a) and the findings of Frauenfelder et al. (2001).

Estimating a characteristic advance rate of 1100 m in 2500 years, a rock glacier width of 150 m (<200 m), a height of 30 m (<40 m), and a debris fraction of 0.6, we arrive at a debris flux $q \approx (150\ m \times 30\ m \times 0.6 \times 1100\ m) / 2500\ a = 1190\ m^3 a^{-1}$ ($<2110\ m^3 a^{-1}$). Spread over the source area, this debris flux theoretically corresponds to head-wall erosion rates of ~3.8–6.8 mm a^{-1}. We hypothesize that such a high debris flux was most likely not in balance with long-term average debris supply rate. Instead, the rapid advance of the debris-ice lobe was enabled and conditioned by debris supplied by the mobilisation of reworked Egesen cirque glacier-derived material (Frauenfelder et al., 2001, 2005) and the warming-induced rapid head wall weathering during the early Holocene (Kenner and Magnusson, 2017). We imagine the lower elevation part of Bleis

Marscha rock glacier as a rapidly down-rushing, short-lived debris pulse (cf. Kirkbride and Brazier, 1995). Our findings of a high rock glacier headwall ratio (Kenner and Magnusson, 2017) despite relatively short activity phase of early Holocene relict inactive rock glaciers (Böhlert et al., 2011a) seems to be representative for the Julier-Albula region.

5.3 Middle Holocene: Slow thermal degradation

After 10 ka, the climate shifted towards warmer conditions (Schimmelpfennig et al., 2014; Solomina et al., 2015) and the lower permafrost boundary began to rise above the rock glacier front at 2400 m a.s.l. (Frauenfelder et al., 2001). By the middle Holocene, the lower continuous permafrost boundary was at least as high as today, likely above 2600 m a.s.l. (present permafrost distribution/ 2°C isotherm, Fig. 3) and likely located near the topographically constrained talus-rock glacier transition in the back of the cirque. The tree line was higher than today (Nicolussi et al., 2005) (Fig. 11).

From the regional climate history, both climatic and dynamic inactivation are conceivable. What drove early Holocene inactivation? The present surface movement pattern and ground ice distribution is correlated with its coarse debris cover which is favourable for cold ground thermal regimes. Immediately below the major inner scarp at 2550 m a.s.l. that separates the transitional inactive early Holocene from the overriding active late Holocene generation, we observe surface speeds of 30–40 cm a^{-1} (magnitudes similar to the upper active lobes), and en-bloc movement of an entire morphologically delineated lobe (unit III, Fig. 4). First, this viscous deformation pattern indicates stress transmission over >100 m and requires the presence of (excess) ground ice – notably beneath an early–middle Holocene boulder mantle that predates the activity phase of the upper lobes by several thousand years. Although the high, active lobe-like deformation susceptibility might be in part explained by higher ground temperatures at lower elevations, mechanical loading exerted by the overriding younger generation (unit IV, Figs. 4, 5a), and greater thickness of the two-generation stack of lobes, the ice content in the lower, transitional inactive lobes must be significant (and mapped as ice-rich permafrost type by Kenner et al. (2019)). Second, a fresh lateral boulder apron (Fig. 5c) shows that the lobe (unit III) began to pour over its own lateral, vegetated outer ridge. This implies recently renewed motion after a long quiet phase where soil could develop, i.e. a forced reactivation (cf. Kirkbride and Brazier, 1995) most likely due to mechanical interaction of lobes. The age of the inferred ground ice is not known and can be original as well as recharged interstitial ice (Giardino and Vitek, 1988; Colucci et al., 2019). From the impression of a still intact-looking micro-topography (Fig. 5b) we believe that the ice is as old as its covering debris mantle and of early Holocene age, otherwise the surface must look more disrupted and collapsed. Self-preservation of ground ice thanks to its high heat capacity and the cooling effect of air circulation in the overlying coarse-debris mantle is a commonly observed phenomenon in rock glaciers (Guodong et al., 2007, Colucci et al., 2019; Kellerer-Pirklbauer, 2019). For example, preservation of early Holocene subsurface ice through the mid-Holocene warm period is interpreted by Krainer et al. (2015) for the the Lazaun rock glacier. In contrast, unlike most of the lower rock glacier lobes, the rock-fall deposits ("radiolarite protrusion", Figs. 3, 5a) show no movement and remained stable despite the mechanical load of the advancing 'rapid lobe'. These parts likely contain no ground ice. As these parts are below fine-grained surface cover (fractured radiolarite, soil,

grassy vegetation; Fig. 12), the local ground thermal regime is less susceptible to permafrost conditions (Harris and Pedersen, 1998; Schneider et al., 2012). This has likely enabled substantial or complete ground ice loss in the past.

Figure 12: View upstream (to E) from the radiolarite debris fall deposits. Coarse debris-covered unit IV (late Holocene age, 'rapid lobe') rapidly advances over unit III (early-middle Holocene). Although overall moving and therefore ground-ice bearing as well, unit III is stable in this corner where it is covered with finer debris of shattered radiolarite and soil (cf. Fig. 9). The boundary between moving and stable areas coincides with the different substrate types. The ground thermal regime under the fine material has not been favourable for ground ice preservation.

Rock glacier degradation is conditioned by the energy fluxes towards the ice-rich permafrost body. Water plays a crucial role as a coupling agent: Water contributes to thermal degradation (thawing) via rapid heat advection and enhances motion (up to mechanical destabilisation) by increasing pore water pressure (Sorg et al., 2015; Wirz et al., 2016; Cicoira et al., 2019). For the low-elevation, early Holocene lobes of Bleis Marscha rock glacier, inactivation extended over several thousand years after emplacement, and is still incomplete. Ongoing movement and the intact micro-topography shows that the relict status is by far not attained. Only the collapsing southernmost corner shows signs of advanced permafrost degradation and ice loss. To stress the slow transition towards a relict state (degradation), we classified the low-elevation lobes as "transitional-inactive" (cf. Giardino and Vitek, 1988). We explain the slow degradation and inactivation of the low-elevation lobes by (i) thermal decoupling from the atmosphere (coarse debris mantle) and (ii) partial hydrological decoupling to upslope area and neighbouring talus (as the lobes rise above adjacent talus slopes).

Two reasonings answer the question "What drove early Holocene inactivation?". First, the presence of azonal ground ice below the -2°C isotherm at 2540 m a.s.l. speaks against climatic inactivation (Fig. 3, lower boundary of discontinuous permafrost (Haeberli, 1985; Colucci et al., 2019)). Second, given the enormous post-YD debris flux likely exceeding the supply rate, it is plausible that the advance ceased as debris storage became exhausted (supply-limited system). Our hypothesis of dominantly dynamic inactivation agrees with modelling studies that find that debris supply governs the long-term development (thickness and advance rate) of rock glaciers (Müller et al., 2016).

5.4 Late Holocene: Intermittent glacier–rock glacier interaction

In the late Holocene, after approximately 4 ka, climate cooled, timberline moved to lower elevations, and glacier advances became more frequent, longer and more severe compared to the middle Holocene (Fig. 11) (Joerin et al., 2006; Ivy-Ochs et al., 2009; Le Roy et al., 2015; Badino et al., 2018 and references therein). The rapidly fluctuating glaciers were forced by climatic instabilities on a centennial timescale, superimposed on a multimillennial-scale cooling trend towards increased glacier extents culminating in the LIA between 1350 and 1850 (Solomina et al., 2016). Increasingly wetter conditions after 4 ka (Zerathe et al., 2014), more frequent glacier advances (Badino et al., 2018), air temperature oscillations and concomitant freeze-thaw cycles weakened the headwall and increased frost shattering and debris production, enhanced by the tectonically weakened fault zone in the headwall (Figs. 3–5a).

Due to the decrease of horizontal speeds with depth and the frontal ice melt-out, the rock glacier surface moves faster than the advancing landform itself ('conveyor belt'-like advance mechanism, Haeberli et al., 1998; Frauenfelder et al., 2005; Kääb and Reichmuth, 2005). The maximum surface exposure age, measured atop the rock glacier front, gives a minimum landform age (e.g. Scapozza et al., 2014). The oldest exposure age (Err11) atop the front of the active upper lobe indicates that the most recent phase of activity phase likely began at or just before 2.8 ± 0.1 ka and lasts until today. According to the dual-threshold model presented in Kirkbride and Brazier (1995), initiation of a new rock glacier lobe occurs when an external climate threshold and an internal shear stress threshold are crossed simultaneously. As the debris reservoir in the Bleis Marscha cirque was replenished since inactivation of the first generation, sufficient internal ice could segregate and super-saturate a sufficiently thick debris accumulation with some lag after onset of the late Holocene cooling. At the moment of onset of viscous creep, a new, second-generation rock glacier lobe was formed.

Long-term average debris fluxes of the late-Holocene generation rock glacier lobe are in the order of 370–810 $m^3 a^{-1}$, calculated from mean speeds of 480 m/2800 a (length of lobe divided by oldest exposure age) and 0.3 m a^{-1} (average speed of last 1200 years), respectively, and a rock-glacier width of 120 m (<150 m), a height of 30 m, and a debris fraction of 0.6. These fluxes correspond to head-wall erosion rates of ~1.2–2.6 mm a^{-1}. Given the massive debris accumulation in the cirque (Fig. 5a), the system must have been transport-limited during the late Holocene active phase, i.e. the debris evacuation rate cannot have exceeded the supply rate by head-wall retreat. In contrast to these long-term average and therefore sustainable debris fluxes, the currently inferred flux on the 'rapid lobe' is likely much higher, $q \approx 120\ m \times 30\ m \times 0.6 \times (0.5 \text{ to } 0.6\ m\ a^{-1}) \approx (1080 \text{ to } 1300\ m^3 a^{-1})$. The discrepancy between currently observed rock glacier fluxes with respect to inferred long-term talus supply rate can be explained by kinematic wave theory (Degenhardt and Giardino, 2003; Müller et al., 2016). The 'rapid lobe' (frontal parts of unit IV) is possibly a surge package (Kenner et al., 2014) or a wave of increased discharge, possibly amplified by the terrain drop-off below the cirque lip (Fig. 5a). It is expressed as a down-stream travelling bulge that propagates faster than the mean surface velocity (Degenhardt and Giardino, 2003). Currently observed surface speeds

~~are temporarily higher than the life-time average and the travel time could be underestimated (Fig. 10). This would bring the outlier sample Err11 towards the 1:1 line (Fig. 10).~~

~~During the late Holocene cold phases, the Bleis Marscha cirque was likely intermittently occupied at the most by a perennial ice patch or a glacieret (Frauenfelder et al, 2005), similar to the LIA extent as mapped in the mid-19th century (Dufour, 1853; Siegfried, 1887; cf. Badino et al., 2018). The ice patch likely never extended beyond the margins of the cirque (Fig. 4). The micro-topography of the lower part has been well preserved throughout the entire Holocene, as it was apparently beneath the lowest limits of any subsequent glacier advances.~~

~~The intact morphology of the active rock glacier lobes (units IV–V), the continuous exposure age progression and the consistent and moderate (~30 cm a^{-1}) magnitudes of short- and long-term creep rates suggest uninterrupted creep for the last ~1200 years without disruptive changes in the dynamics or thermal state. Permafrost conditions have likely been relatively stable in the high-elevation (>2700 m a.s.l.) cirque despite the climate oscillations of the last 1200 years. This is plausible given the fact that the shadowed cirque floor is in the continuous permafrost belt even today (Gruber et al., 2006; Boeckli et al., 2012). Although the debris provenance of the Bleis Marscha rock glacier (Err granodiorite) is in the headwall behind the now-gone glacieret and there must have been glacier–rock glacier interaction, the rock glacier is clearly older than the LIA glacieret. Despite the likely incorporation of sedimentary ice and glacial debris, the Bleis Marscha rock glacier is not a glacier-derived rock glacier that has transformed from a LIA ice glacier. Instead, weak morphological evidence of the presence of the glacieret suggests that the small glacieret was stagnant or thin. The late Holocene cirque glaciers could not destroy the rock glacier; permafrost and the pre-existing rock glacier outlasted beneath the ice patch and were not disrupted by the presence of the glacieret, agreeing with Frauenfelder et al. (2001, 2005) and Kenner et al. (2018). The reason for these stable permafrost conditions during the entire lifetime of the Bleis Marscha active rock glacier lobes might be the very permafrost-friendly, shadowy, high-elevation cirque with sparse glaciation during the late Holocene (Dufour, 1853). The Bleis Marscha rock glacier root at an elevation above 2650 m a.s.l. is even now (in a relatively warm climate) above the permafrost limit and must have been so during extended periods of the late Holocene (Gruber et al., 2006; Boeckli et al., 2012). During LIA-like cold pulses of the late Holocene, the lower limit of permafrost was depressed by many tens of meters (Frauenfelder et al., 2001). This is a very favourable environment for ice preservation and slow, steady rock glacier growth. With the late Holocene climatic oscillations (oscillating ELA), the dominant coarse-debris transport mechanism in the rear part of Bleis Marscha cirque alternated between a "conveyor-belt like" glacial transport during cold phases and permafrost creep during glacial ice-free "mild" phases (Zasadni, 2005; Kenner et al., 2018). Ice of glacial and non-glacial sources might have been incorporated. During the late Holocene, the continuously growing rock glacier intermittently coexisted with a fluctuating cirque glacieret.~~

6. Conclusions

We constrained ~~activity~~ formation phases and reconstructed the ~~morphodynamic~~ development of the active Bleis Marscha rock glacier (Val d'Err, eastern Switzerland) with morphostratigraphic relations from field observations, 15 cosmogenic nuclide exposure ages (14 ^{10}Be and 1 ^{36}Cl sample), ~~and present~~ modern (2003/2012) surface creep quantification from aerial image correlation, and ~~.~~finite element modelling to separate the control of topography and ice content on surface movement. In contrast to earlier works that exposure dated relict rock glaciers, the Bleis Marscha lobes are presently active. Boulder nuclide inventories are stochastically overprinted primarily by the cumulative effect of small instabilities while travelling on the rock glacier surface. This leads to tendentially 'too young' exposure ages, although bedrock inheritance ('too old') cannot be excluded in individual cases. The correlation of two orthophotos from 2003 and 2012 indicates average movement at creep rates of 25–60 cm a^{-1}. ~~–~~Bleis Marscha is a 1100 m long, active, polymorphic talus rock glacier at an elevation range of 2400~~ – to –~~2700 m a.s.l~~., with active upper lobes and transitional inactive lower lobes~~.~~ – Coinciding ~~Morphological~~ morphological discontinuities (terrain steps~~steep scarps~~) ~~coinciding with~~and kinematic discontinuities (decorrelation gaps, velocity jumps)~~, and two distinct exposure age populations indicate that~~separate the Bleis Marscha rock glacier ~~is~~ in ~~composed~~ a stack of three lobes, each with its own formation phase. Our cosmogenic nuclide data suggest that the birth of each of the three lobes appears to correlate with Holocene climate shifts: Early Holocene, ~8.9–8.0 ka; Middle Holocene, ~5.2–4.8 ka; and Late Holocene, since ~2.8 ka.~~two distinct groups of lobes linked to two activity phases in the early and late Holocene, separated by a middle Holocene period of inactivation and quiescence.~~

~~The low-elevation older generation formed during the late Younger Dryas and persisted into the early Holocene in a short time frame of a favourable succession of climatic conditions: First, an aridification at still cold conditions during the late Younger Dryas, leading to glacier starvation, retreat, and permafrost growth, later followed by significant warming at around 10 ka. Crosscutting relationships in the field suggest that the rock glacier formed after the retreat of the Egesen Bleis Marscha cirque glacier. The six ^{10}Be ages for the older generation lobes have a large dispersion and show no correlation to downstream distance. Exposure age dispersion and inversions for a single inactive lobe reflects settling and decay during inactivation, affecting the nuclide inventory of boulders randomly and independently. We interpret these ages as inactivity or stabilisation ages. The oldest age from a boulder atop the lowermost front places the end of the activity phase at no later than 8.9 ± 0.5 ka.~~ Crosscutting relationships in the field indicate that the low-elevation, early Holocene generation of Bleis Marscha rock glacier formed after the retreat of the Egesen Bleis Marscha glacier, with exposure ages pointing at ~8.9–8.0 ka. The rapid buildup of voluminous rock glacier bodies in the rapidly warming climate of the early Holocene was likely conditioned by warming-induced high rock-fall activity. ~~The rapid emplacement (1100 m within ~2500 years) of the early Holocene generation was enabled by high debris fluxes likely exceeding a sustainable supply rate. It evacuated previously accumulated Egesen glacier derived debris, whose exhaustion ultimately lead to stagnation and cessation of the advance. The pulse-like behaviour in the early Holocene warming climate and the incorporation of glacial and non-glacial material agrees with previous studies on the Bleis Marscha rock glacier.~~The end of the formation phase could be linked to insufficient

or imbalanced supply of debris and ice in proportions no longer susceptible for rock glacier creep. The mid-Holocene generation formed at ~5.2–4.8 ka during a dominantly warm period interrupted by short cold spells as documented by glacier advances.

~~Ongoing coherent surface deformation and settling governed by the small-scale micro-topography on the morphologically transitional-inactive lobes requires the presence of ground ice as stress transmitter beneath the early Holocene boulder mantle. Although these lobes are below the current -2°C isotherm, we believe from the still intact micro-topography that the ice is original, preserved from the early Holocene. Thermally driven inactivation of this azonal, ice-rich permafrost body, in contrast to its rapid emplacement, has been slow and is still incomplete. Therefore, dynamic rather than climatic inactivation caused the rock glacier to stall. Due to the high heat capacity of ice-rich material, the thermal decoupling and ground cooling provided by the coarse-debris mantle, sufficiently stable permafrost conditions were maintained even during the middle Holocene warm phase.~~

The formation phase of the high-elevation ~~younger~~ youngest late Holocene generation likely began at ~2.8 ka as indicated by its oldest exposure age atop the front, roughly coeval with the onset of the late Holocene climate oscillations. Although these lobes are sourced in the during late Holocene intermittently glacierized Bleis Marscha cirque, their morphological continuity suggests undisturbed growth~~developed from the late Holocene until today. The oldest exposure age atop the front of the active upper lobe indicates that the most recent phase of activity phase likely began before 2.8 ± 0.1 ka. This late Holocene rock glacier advanced by 460 m in 3000 years and involved moderate and most likely sustainable debris fluxes. The nine exposure ages show a small dispersion and correlate linearly with down-stream distance. This suggests undisturbed creep at an average rate of 30 cm a^{-1} during the last ~1200 years, a rate that is consistent with present short-term 2003/2012 creep rates we determined. Furthermore, travel time estimates from streamline interpolations agree well with the exposure ages. The rock glacier lobes developed uninterruptedly under stable permafrost conditions despite the climatic oscillations during the Medieval Warm Period, LIA, and the current warming up to now~~. Due to favourable topo-climatic conditions in the ~~shadowy,~~ high-elevation cirque (>2650 m a.s.l., ~~above the~~MAAT ~~-~~2°C ~~isotherm~~) and ~~polythermal-cold based~~small, stagnant cirque glacieret~~s~~, ground thermal conditions in the ~~rock glacier~~rock glacier root zone remained cryotic and~~-~~ interactions with the glacieret were not disruptive for the rock glacier development. ~~despite late Holocene climate oscillations. Our data from the active lobes of the Bleis Marscha rock glacier show that exposure ages for rock glacier lobes that are presently active and have not experienced disruptive dynamic changes during their lifetime can be interpreted as (minimum) travel times. Notably, it also shows that pre-travel nuclide build-up is insignificant. The rock glacier is sourced in the during late Holocene intermittently glacierized Bleis Marscha cirque. Even during the LIA glacier high stand, interactions with the cirque glacieret were not disruptive for the rock glacier development. The Bleis Marscha rock glacier predates the LIA glacieret, which however does not exclude the incorporation of glacier-derived material (debris and ice).~~

Ongoing cohesive surface deformation on old, early- and mid-Holocene Bleis Marscha lobes requires the presence of ice as stress transmitter. Although these lobes are below the current -2°C isotherm, we believe from the intact microtopography that the ice is largely original, preserved from the early/middle Holocene. Degradation of this azonal, ice-rich permafrost body, in contrast to its rapid formation, is slow and attenuated by the debris mantle. We find contrasting responses to external forcing of Bleis Marscha rock glacier parts: The successive initiation of three lobes in the Holocene suggests that rock glacier formation processes in the Bleis Marscha cirque were climate-sensitive, enabled by high rock-fall activity so that debris availability is not a limiting factor. Contrariwise, once formed, the boulder-mantled, ice-rich lobes reacted less sensitively to climate forcing, with permafrost degradation protracted over millennia.~~Although the two rock-glacier generations originated in the same cirque, we find contrasting responses to external forcing by comparing typical advance rates and debris flux estimates for both rock glacier generations. This very different dynamic history of the two rock glacier generations is expressed in the exposure age distributions of the different lobes.~~

~~*Code availability*. The code used for flowline and strain-rate calculations is available by request from the corresponding author.~~

Author contributions. S.I.-O., O.S., and M.F. designed the study. D.A., S.I.-O., O.S. and M.F. conducted the field work. O.S and D.A. carried out the ^{10}Be extraction, O.S. ~~and C.V.~~ the ^{36}Cl extraction, and M.C. with C.V. the AMS measurements. D.A. computed the image correlation. D.A. and M.F. did the finite~~-~~ element modelling. D.A. prepared the figures and the manuscript which were edited by S.I.-O., O.S. and M.F.

Acknowledgements. We are grateful for the field support by Ueli Steinemann, Reto Grischott and Jonas von Wartburg. We thank Kristina Hippe and Ewelina Bros for their assistance during sample preparation and the Laboratory of Ion Beam Physics group for excellent AMS measurements. We thank Armando Janett (~~local~~ gamekeeper in municipality Surses), Carole Müller, and Peter Kaiser (Savognin) for their logistical support, and Reynald Delaloye (University of Fribourg) for the geomorphological discussions.~~.~~

Financial support. D. Amschwand received financial support for the fieldwork by the Swiss Society for Quaternary Research. This work was completed in the framework of Swiss National Science Foundation project (SNF) 175794.

Competing interests. The authors declare that they have no conflict of interest.

References

Alfimov, V. and Ivy-Ochs, S.: How well do we understand production of ^{36}Cl in limestone and dolomite?, Quat Geochronol, 4, 462–474, https://doi.org/10.1016/j.quageo.2009.08.005, 2009.

Anderson, R. S., Anderson, L. S., Armstrong, W. H., Rossi, M. W., and Crump, S. E.: Glaciation of alpine valleys: The glacier – debris-covered glacier – rock glacier continuum, Geomorphology, 311, 127–142, https://doi.org/10.1016/j.geomorph.2018.03.015, 2018.

Arenson, L., Hoelzle, M., and Springman, S.: Borehole deformation measurements and internal structure of some rock glaciers in Switzerland, Permafrost Periglac, 13, 117–135, https://doi.org/10.1002/ppp.414, 2002.

~~Arenson, L. U., Kääb, A., and O'Sullivan, A.: Detection and analysis of ground deformation in permafrost environments, Permafrost Periglac, 27, 339–351, https://doi.org/10.1002/ppp.1932, 2016.~~

Badino, F., Ravazzi, C., Vallè, F., Pini, R., Aceti, A., Brunetti, M., Champvillair, E., Maggi, V., Maspero, F., Perego, R., and Orombelli, G.: 8800 years of high-altitude vegetation and climate history at the Rutor Glacier forefield, Italian Alps. Evidence of middle Holocene timberline rise and glacier contraction, Quaternary Sci Rev, 185, 41–68, https://doi.org/10.1016/j.quascirev.2018.01.022, 2018.

Balco, G., Stone, J. O., Lifton, N. A., and Dunai, T. J.: A complete and easily accessible means of calculating surface exposure ages or erosion rates from ^{10}Be and ^{26}Al measurements, Quat Geochronol, 3, 174–195, https://doi.org/10.1016/j.quageo.2007.12.001, 2008.

Barsch, D.: Rockglaciers. Indicators for the Present and Former Geoecology in High Mountain Environments, Springer series in physical environment vol. 16, Springer, Berlin, Heidelberg, https://doi.org/10.1007/978-3-642-80093-1, 1996.

Bini, A., Buoncristiani, J.-F., Couterrand, S., Ellwanger, D., Felber, M., Florineth, D., Graf, H., Keller, O., Kelly, M., Schlüchter, C., and Schoeneich, P.: Die Schweiz während des letzteiszeitlichen Maximums (LGM) 1:500'000, Bundesamt für Landestopographie (swisstopo), Wabern, https://opendata.swiss/en/dataset/die-schweiz-wahrend-des-letzteiszeitlichen-maximums-lgm-1-500000, 2009.

Biot, M. A.: Theory of folding of stratified viscoelastic media and its implications in tectonics and orogenesis, GSA Bulletin, 72, 1595–1620, https://doi.org/10.1130/0016-7606(1961)72[1595:TOFOSV]2.0.CO;2, 1961.

Bodin, X., Krysiecki, J.-M., Schoeneich, P., Le Roux, O., Lorier, L., Echelard, T., Peyron, M., and Walpersdorf, A.: The 2006 collapse of the Bérard rock glacier (southern French Alps), Permafrost Periglac, 28, 209–223, https://doi.org/10.1002/ppp.1887, 2016.

Boeckli, L., Brenning, A., Gruber, S., and Noetzli, J.: Permafrost distribution in the European Alps: Calculation and evaluation of an index map and summary statistics (Alpine permafrost index map, APIM), The Cryosphere, 6, 807–820, https://doi.org/10.5194/tc-6-807-2012, 2012.

Bohleber, P., Schwikowski, M., Stocker-Waldhuber, M., Fang, L., and Fischer, A.: New glacier evidence for ice-free summits during the life of the Tyrolean Iceman, Sci Rep, 10, 20513, https://doi.org/10.1038/s41598-020-77518-9, 2020.

Böhlert, R., Compeer, M., Egli, M., Brandová, D., Maisch, M., W Kubik, P., and Haeberli, W.: A combination of relative-numerical dating methods indicates two high Alpine rock glacier activity phases after the glacier advance of the Younger Dryas, The Open Geography Journal, 4, 115–130, https://doi.org/10.2174/1874923201003010115, 2011a.

Böhlert, R., Egli, M., Maisch, M., Brandová, D., Ivy-Ochs, S., Kubik, P. W., and Haeberli, W.: Application of a combination of dating techniques to reconstruct the Lateglacial and early Holocene landscape history of the Albula region (eastern Switzerland), Geomorphology, 127, 1–13, https://doi.org/10.1016/j.geomorph.2010.10.034, 2011b.

Chandler, B. M. P., Lovell, H., Boston C. M., Lukas, S., Barr, I. D., Benediktsson, I. Ö., Benn, D. I., Clark, C. D., Darvill, C. M., Evans, D. J. A., Ewertowski, M. W., Loibl, D., Margold, M., Otto, J.-C., Roberts, D. H., Stokes, C. R., Storrar, R. D., and Stroeven, A. P.: Glacial geomorphological mapping: A review of approaches and frameworks for best practice, Earth-Sci Rev, 185, 806–846, https://doi.org/10.1016/j.earscirev.2018.07.015, 2018.

Christl, M., Vockenhuber, C., Kubik, P., Wacker, L., Lachner, J., Alfimov, V., and Synal, H.-A.: The ETH Zurich AMS facilities: Performance parameters and reference materials, Nuclear Instruments and Methods in Physics Research Section B: Beam Interactions with Materials and Atoms, 294, 29–38, https://doi.org/10.1016/j.nimb.2012.03.004, 2013.

Cicoira, A., Beutel, J., Faillettaz, J., and Vieli, A.: Water controls the seasonal rhythm of rock glacier flow, Earth Planet Sc Lett, 528, 115-844, https://doi.org/10.1016/j.epsl.2019.115844, 2019.

Cicoira, A., Marcer, M., Gärtner-Roer, I., Bodin, X., Arenson, L., and Vieli, A.: A general theory of rock glacier creep based on in-situ and remote sensing observations, Permafrost Periglac, 1–15, https://doi.org/10.1002/ppp.2090, 2020.

Claude, A., Ivy-Ochs, S., Kober, F., Antognini, M., Salcher, B., and Kubik, P. W.: The Chironico landslide (Valle Leventina, southern Swiss Alps): Age and evolution, Swiss J Geosci, 107, 273–291, https://doi.org/10.1007/s00015-014-0170-z, 2014.

Colucci, R. R., Forte, E., Žebre, M., Maset, E., Zanettini, C., and Guglielmin, M.: Is that a relict rock glacier?, Geomorphology, 330, 177–189, https://doi.org/10.1016/j.geomorph.2019.02.002, 2019.

~~Cornelius, H. P.: Geologie der Err-Julier-Gruppe (Erläuterungen zur Spezialkarte Nr. 115). 1. Teil: Das Baumaterial (Stratigraphie und Petrographie, excl. Quartär), Beiträge zur Geologischen Karte der Schweiz, Nr. 70.1, 1935.~~

~~Cornelius, H. P.: Geologie der Err-Julier-Gruppe (Erläuterungen zur Spezialkarte Nr. 115). 2. Teil: Der Gebirgsbau, Beiträge zur Geologischen Karte der Schweiz, Nr. 70.2, 1950.~~

Cornelius, H.P.: Geologische Karte der Err-Julier-Gruppe 1:25 000, 2 Blätter. Beitr. Geol. Karte Schweiz, Spezialkarte Nr. 115 A (Westblatt), 1932.

Crump, S. E., Miller, G. H., and Anderson, R. S.: Interpreting exposure ages from ice-cored moraines: a Neoglacial case study on Baffin Island, Arctic Canada, J Quaternary Sci, 32, 1049–1062, https://doi.org/10.1002/jqs.2979, 2017.

~~D'Errico, J.: inpaint_nans 1.1.0.0, MATLAB Central File Exchange, https://www.mathworks.com/matlabcentral/fileexchange/4551-inpaint_nans, 2012.~~

Debella-Gilo, M. and Kääb, A.: Locally adaptive template sizes for matching repeat images of Earth surface mass movements, ISPRS J Photogramm, 69, 10–28, https://doi.org/10.1016/j.isprsjprs.2012.02.002, 2012.

~~Denn, A. R., Bierman, P. R., Zimmerman, S. R. H., Caffee, M. W., Corbett, L. B., and Kirby, E.: Cosmogenic nuclides indicate that boulder fields are dynamic, ancient, multigenerational features, GSA Today, 28, 4–10, https://doi.org/10.1130/GSATG340A.1, 2017.~~

Degenhardt Jr., J. J. and Giardino, J. R.: Subsurface investigation of a rock glacier using ground-penetrating radar: Implications for locating stored water on Mars, J Geophys Res-Planet, 108, https://doi.org/10.1029/2002JE001888, 2003.

Delaloye, R., Lambiel, C., and Gärtner-Roer, I.: Overview of rock glacier kinematics research in the Swiss Alps, Geographica Helvetica, 65, 135–145, https://doi.org/10.5194/gh-65-135-2010, 2010.

Delaloye, R., Barboux, C., Bodin, X., Brenning, A., Hartl, L., Hu, Y., Ikeda, A., Kaufmann, V., Kellerer-Pirklbauer, A., Lambiel, C., Liu, L., Marcer, M., Rick, B., Scotti, R., Takadema, H., Trombotto Liaudat, D., Vivero, S., and Winterberger, M.: Rock glacier inventories and kinematics: A new IPA Action Group, in: Proceedings of the 5th European Conference on Permafrost, Chamonix-Mont Blanc, France, 23 June–1 July 2018, 392–393, 2018.

Deline, P. and Orombelli, G.: Glacier fluctuations in the western Alps during the Neoglacial, as indicated by the Miage morainic amphitheatre (Mont Blanc massif, Italy), Boreas, 34, 456–467, https://doi.org/10.1111/j.1502-3885.2005.tb01444.x, 2005.

Formatiert: Englisch (Vereinigte Staaten)

Feldfunktion geändert

Dufour, G.-H.: Topographische Karte der Schweiz, Blatt XV: Davos, Martinsbruck, Eidgenössische Landestopographie, Bern, 1853.

Fernández-Fernández, J. M., Palacios, D., Andrés, N., Schimmelpfennig, I., Tanarro, L. M., Brynjólfsson, S., López-Acevedo, F. J., Þorsteinn Sæmundsson, and A.S.T.E.R. Team: Constraints on the timing of debris-covered and rock glaciers: An exploratory case study in the Hólar area, northern Iceland, Geomorphology, 361, 107 196, https://doi.org/10.1016/j.geomorph.2020.107196, 2020.

Fitch, A. J., Kadyrov, A., Christmas, W. J., and Kittler, J.: Orientation correlation, in: Proceedings of the 13th British Machine Vision Conference, Cardiff, United Kingdom, 2–5 September 2002, 133–142, http://citeseerx.ist.psu.edu/viewdoc/summary?doi=10.1.1.64.5662, 2002.

Frauenfelder, R. and Kääb, A.: Towards a palaeoclimatic model of rock-glacier formation in the Swiss Alps, Ann Glaciol, 31, 281–286, https://doi.org/10.3189/172756400781820264, 2000.

Frauenfelder, R., Haeberli,W., Hoelzle, M., and Maisch, M.: Using relict rockglaciers in GIS-based modelling to reconstruct Younger Dryas permafrost distribution patterns in the Err-Julier area, Swiss Alps, Norsk Geogr Tidsskr, 55, 195–202, https://doi.org/10.1080/00291950152746522, 2001.

Frauenfelder, R., Laustela, M., and Kääb, A.: Relative age dating of Alpine rockglacier surfaces, Z Geomorphol, NF, 49, 145–166, 2005.

Frehner, M., Ling, A. H. M., and Gärtner-Roer, I.: Furrow-and-ridge morphology on rockglaciers explained by gravity-driven buckle folding: A case study from the Murtèl rockglacier (Switzerland), Permafrost Periglac, 26, 57–66, https://doi.org/10.1002/ppp.1831, 2015.

Giardino, J. R. and Vitek, J. D.: The significance of rock glaciers in the glacial-periglacial landscape continuum, J Quaternary Sci, 3, 97–103, https://doi.org/10.1002/jqs.3390030111, 1988.

Gruber, S., Haeberli,W., Krummenacher, B., Keller, F., Mani, P., Hunziker, G., Hölzle, M., Vonder Mühll, D., Zimmermann, M., Keusen, H.-R., Götz, A., and Raetzo, H.: Erläuterungen zur Hinweiskarte der potentiellen Permafrostverbreitung in der Schweiz 1:50'000 (potential permafrost distribution map, PPDM), Bundesamt für Umwelt (BAFU), Bern, 2006.

~~Guodong, C., Yuanming, L., Zhizhong, S., and Fan, J.: The 'thermal semi-conductor' effect of crushed rocks, Permafrost Periglac, 18, 151–160, https://doi.org/10.1002/ppp.575, 2007.~~

Haeberli, W.: Creep of mountain permafrost: Internal structure and flow of Alpine rock glaciers, Mitteilungen der Versuchsanstalt für Wasserbau, Hydrologie und Glaziologie (VAW) an der ETH Zürich vol. 77, 1985.

Haeberli, W., Hoelzle, M., Kääb, A., Keller, F., Vonder Mühll, D., and Wagner, S.: Ten years after drilling through the permafrost of the active rock glacier Murtèl, Eastern Swiss Alps: Answered questions and new perspectives, in: Proceedings of the 7th International Conference on Permafrost, Yellowknife, Northwest Territories, Canada, 23–27 June 1998, 403–410, 1998.

Haeberli, W., Brandova, D., Burga, C., Egli, M., Frauenfelder, R., Kääb, A., Maisch, M., Mauz, B., and Dikau, R.: Methods for absolute and relative age dating of rock-glacier surfaces in Alpine permafrost, in: Proceedings of the 8th International Conference on Permafrost, Zürich, Switzerland, 21–25 July 2003, vol. 1, 343–348, 2003.

Haeberli, W., Hallet, B., Arenson, L., Elconin, R., Humlum, O., Kääb, A., Kaufmann, V., Ladanyi, B., Matsuoka, N., Springman, S., and Vonder Mühll, D.: Permafrost creep and rock glacier dynamics, Permafrost Periglac, 17, 189–214, https://doi.org/10.1002/ppp.561, 2006.

Haeberli, W., Schaub, Y., and Huggel, C.: Increasing risks related to landslides from degrading permafrost into new lakes in deglaciating mountain ranges, Geomorphology, 293, 405–417, https://doi.org/10.1016/j.geomorph.2016.02.009, 2017.

Hanson, S. and Hoelzle, M.: The thermal regime of the active layer at the Murtèl rock glacier based on data from 2002, Permafrost Periglac, 15, 273–282, https://doi.org/10.1002/ppp.499, 2004.

Formatiert: Deutsch (Schweiz)

Feldfunktion geändert

Formatiert: Deutsch (Schweiz)

Formatiert: Deutsch (Schweiz)

Harris, S. A. and Pedersen, D. E.: Thermal regimes beneath coarse blocky materials, Permafrost Periglac, 9, 107–120, https://doi.org/10.1002/(SICI)1099-1530(199804/06)9:2<107::AID-PPP277>3.0.CO;2-G, 1998.

Heyman, J., Stroeven, A. P., Harbor, J. M., and Caffee, M. W.: Too young or too old: Evaluating cosmogenic exposure dating based on an analysis of compiled boulder exposure ages, Earth Planet Sc Lett, 302, 71–80, https://doi.org/10.1016/j.epsl.2010.11.040, 2011.

Hock, R., Rasul, G., Adler, C., Cáceres, B., Gruber, S., Hirabayashi, Y., Jackson, M., Kääb, A., Kang, S., Kutuzov, S., ,Milner, Al., Molau, U., Morin, S., Orlove, B., and Steltzer, H.: High mountain areas, in: IPCC Special Report on the Ocean and Cryosphere in a Changing Climate, edited by: Pörtner, H.-O., Roberts, D.C., Masson-Delmotte, V., Zhai, P., Tignor, M., Poloczanska, E., Mintenbeck, K., Alegría, A., Nicolai, M., Okem, A., Petzold, J., Rama, B., Weyer, N.M., 131–202, 2019.

Holzhauser, H., Magny, M., and Zumbühl, H. J.: Glacier and lake-level variations in west-central Europe over the last 3500 years, The Holocene, 15, 789–801, https://doi.org/10.1191/0959683605hl853ra, 2005.

Humlum, O.: The climatic significance of rock glaciers, Permafrost Periglac, 9, 375–395, https://doi.org/10.1002/(SICI)1099-1530(199810/12)9:4<375::AID-PPP301>3.0.CO;2-0, 1998.

Ivy-Ochs, S.: Glacier variations in the European Alps at the end of the last glaciation, Cuadernos de Investigación Geográfica, 41, 295–315, https://doi.org/10.18172/cig.2750, 2015.

Ivy-Ochs, S., Kerschner, H., and Schlüchter, C.: Cosmogenic nuclides and the dating of Lateglacial and Early Holocene glacier variations: the Alpine perspective. Quatern Int, 164, 53–63, https://doi.org/10.1016/j.quaint.2006.12.008, 2007.

Ivy-Ochs, S. and Kober, F.: Surface exposure dating with cosmogenic nuclides, Quaternary Science Journal, 57, 179–209, https://www.eg-quaternary-sci-j.net/57/179/2008/, 2008.

Ivy-Ochs, S., Synal, H.-A., Roth, C., and Schaller, M.: Initial results from isotope dilution for Cl and ^{36}Cl measurements at the PSI/ETH Zurich AMS facility, Nuclear Instruments and Methods in Physics Research Section B: Beam Interactions with Materials and Atoms, 223-224, 623–627, https://doi.org/10.1016/j.nimb.2004.04.115, 2004.

Ivy-Ochs, S., Kerschner, H., Maisch, M., Christl, M., Kubik, P. W., and Schlüchter, C.: Latest Pleistocene and Holocene glacier variations in the European Alps, Quaternary Sci Rev, 28, 2137–2149, https://doi.org/10.1016/j.quascirev.2009.03.009, 2009.

Joerin, U. E., Stocker, T. F., and Schlüchter, C.: Multicentury glacier fluctuations in the Swiss Alps during the Holocene, The Holocene, 16, 697–704, https://doi.org/10.1191/0959683606hl964rp, 2006.

Jones, D. B., Harrison, S., Anderson, K., and Whalley, W. B.: Rock glaciers and mountain hydrology: A review, Earth-Sci Rev, 193, 66–90, https://doi.org/10.1016/j.earscirev.2019.04.001, 2019.

Kääb, A. and Reichmuth, T.: Advance mechanisms of rock glaciers, Permafrost Periglac, 16, 187–193, http://dx.doi.org/10.1002/ppp.507, 2005.

Kääb, A., Haeberli, W., and Gudmundsson, G. H.: Analysing the creep of mountain permafrost using high precision aerial photogrammetry: 25 years of monitoring Gruben rock glacier, Swiss Alps, Permafrost Periglac, 8, 409–426, https://doi.org/10.1002/(SICI)1099-1530(199710/12)8:4<409::AID-PPP267>3.0.CO;2-C, 1997.

Kaufman, D., McKay, N., Routson, C., Erb, E., Dätwyler, C., Sommer, P. S., Heiri, O., and Davis, B.: Holocene global mean surface temperature, a multi-method reconstruction approach, Sci Data, 7, https://doi.org/10.1038/s41597-020-0530-7, 2020.

Kellerer-Pirklbauer, A.: Long-term monitoring of sporadic permafrost at the eastern margin of the European Alps (Hochreichart, Seckauer Tauern range, Austria), Permafrost Periglac, 30, 260–277, https://doi.org/10.1002/ppp.2021, 2019.

Kenner, R.: Geomorphological analysis on the interaction of Alpine glaciers and rock glaciers since the Little Ice Age, Land Degrad Dev, 30, 580–591, https://doi.org/10.1002/ldr.3238, 2018.

Kenner, R. and Magnusson, J.: Estimating the effect of different influencing factors on rock glacier development in two regions in the Swiss Alps, Permafrost Periglac, 28, 195–208, https://doi.org/10.1002/ppp.1910, 2017.

Kenner, R., Bühler, Y., Delaloye, R., Ginzler, C., and Phillips, M.: Monitoring of high Alpine mass movements combining laser scanning with digital airborne photogrammetry, Geomorphology, 206, 492–504, https://doi.org/10.1016/j.geomorph.2013.10.020, 2014.

Kenner, R.; Noetzli, J.; Hoelzle, M.; Raetzo, H. and Phillips, M.: Distinguishing ice-rich and ice-poor permafrost to map ground temperatures and ground ~~ground ice~~ice occurrence in the Swiss Alps, The Cryosphere, 13, 1925–1941, https://doi.org/10.5194/tc-13-1925-2019, 2019

Kerschner, H. and Ivy-Ochs, S.: Palaeoclimate from glaciers: Examples from the Eastern Alps during the Alpine Lateglacial and early Holocene, Global Planet Change, 60, 58–71, https://doi.org/10.1016/j.gloplacha.2006.07.034, 2008.

Kirkbride, M. and Brazier, V.: On the sensitivity of Holocene talus-derived rock glaciers to climate change in the Ben Ohau Range, New Zealand, J Quaternary Sci, 10, 353–365, https://doi.org/10.1002/jqs.3390100405, 1995.

Knight, J., Harrison, S., and Jones, D. B.: Rock glaciers and the geomorphological evolution of deglacierizing mountains, Geomorphology, 324, 14–24, https://doi.org/10.1016/j.geomorph.2018.09.020, 2019.

Krainer, K., Bressan, D., Dietre, B., Haas, J. N., Hajdas, I., Lang, K., Mair, V., Nickus, U., Reidl, D., Thies, H., and Tonidandel, D.: A 10,300-year-old permafrost core from the active rock glacier Lazaun, southern Ötztal Alps (South Tyrol, northern Italy), Quaternary Res, 83, 324–335, https://doi.org/10.1016/j.yqres.2014.12.005, 2015.

Kronig, O., Ivy-Ochs, S., Hajdas, I., Christl, M., Wirsig, C., and Schlüchter, C.: Holocene evolution of the Triftje- and the Oberseegletscher (Swiss Alps) constrained with ^{10}Be exposure and radiocarbon dating, Swiss J Geosci, https://doi.org/10.1007/s00015-017-0288-x, 2018.

Kutschera, W., Patzelt, G., Steier, P., and Wild, E.: The Tyrolean Iceman and his glacial environment during the Holocene, Radiocarbon, 59, 395–405, https://doi.org/10.1017/RDC.2016.70, 2017.

Lal, D.: Cosmic ray labeling of erosion surfaces: in situ nuclide production rates and erosion models, Earth Planet Sc Lett, 104, 424–439, https://doi.org/10.1016/0012-821X(91)90220-C, 1991.

Lambiel, C. and Delaloye, R.: Contribution of real-time kinematic GPS in the study of creeping mountain permafrost: examples from the Western Swiss Alps. Permafrost Periglac, 15, 229–241, https://doi.org/10.1002/ppp.496, 2004.

Laustela, M., Egli, M., Frauenfelder, R., Kääb, A., Maisch, M., and Haeberli, W.: Weathering rind measurements and relative age dating of rockglacier surfaces in crystalline regions of the Eastern Swiss Alps, in: Proceedings of the 8th International Conference on Permafrost, Zürich, Switzerland, 21–25 July 2003, 627–632, 2003.

Le Roy, M., Nicolussi, K., Deline, P., Astrade, L., Edouard, J.-L., Miramont, C., and Arnaud, F.: Calendar-dated glacier variations in the western European Alps during the Neoglacial: the Mer de Glace record, Mont Blanc massif, Quaternary Sci Rev, 108, 1–22, https://doi.org/10.1016/j.quascirev.2014.10.033, 2015.

~~Leemann, A. and Niessen, F.: Holocene glacial activity and climatic variations in the Swiss Alps: reconstructing a continuous record from proglacial lake sediments, The Holocene, 4, 259–268, https://doi.org/10.1177/095968369400400305, 1994.~~

Marcer, M., Serrano, C., Brenning, A., Bodin, X., Goetz, J., and Schoeneich, P.: Evaluating the destabilization susceptibility of active rock glaciers in the French Alps, The Cryosphere, 13, 141–155, https://doi.org/10.5194/tc-13-141-2019, 2019.

Messerli, A. and Grinsted, A.: Image georectification and feature tracking toolbox: ImGRAFT, Geosci Instrum Meth, 4, 23–34, https://doi.org/10.5194/gi-4-23-2015, 2015.

Mohadjer, S., Ehlers, T.A., Nettesheim, M, Ott, M.B., Glotzbach, C., and Drews, R.: Temporal variations in rockfall and rock-wall retreat rates in a deglaciated valley over the past 11 k.y., Geology, 48, 594–598, https://doi.org/10.1130/G47092.1, 2020.

Moore, P. L.: Deformation of debris-ice mixtures, Rev Geophys, 52, 435–467, https://doi.org/10.1002/2014RG000453, 2014.

Moran, A. P., Ivy-Ochs, S., Vockenhuber, C., and Kerschner, H.: Rock glacier development in the Northern Calcareous Alps at the Pleistocene-Holocene boundary, Geomorphology, 273, 178–188, https://doi.org/10.1016/j.geomorph.2016.08.017, 2016.

Müller, J., Vieli, A., and Gärtner-Roer, I.: Rock glaciers on the run – understanding rock glacier landform evolution and recent changes from numerical flow modeling, The Cryosphere, 10, 2865–2886, https://doi.org/10.5194/tc-10-2865-2016, 2016.

Nicolussi, K., Kaufmann, M., Patzelt, G., Thurner, A., van der Plicht, J., and Thurner, A.: Holocene tree-line variability in the Kauner Valley, Central Eastern Alps, indicated by dendrochronological analysis of living trees and subfossil logs, Veg Hist Archaeobot, 14, 221–234, https://doi.org/10.1007/s00334-005-0013-y, 2005.

Noetzli, J., Pellet, C., and Staub, B. (Eds.): PERMOS 2019. Permafrost in Switzerland 2014/2015 to 2017/2018., Glaciological Report (Permafrost) No. 16–19 of the Cryospheric Commission of the Swiss Academy of Sciences, 104 pp., https://doi.org/10.13093/permos-rep-2019-16-19, 2019.

Nye, J. F.: The Mechanics of Glacier Flow, J Glaciol, 2, 82–93, https://doi.org/10.3189/S0022143000033967, 1952.

Scapozza, C., Lambiel, C., Bozzini, C., Mari, S., and Conedera, M.: Assessing the rock glacier kinematics on three different timescales: A case study from the southern Swiss Alps, Earth Surf Proc Land, 39, 2056–2069, https://doi.org/10.1002/esp.3599, 2014.

Schimmelpfennig, I., Schaefer, J. M., Akçar, N., Koffman, T., Ivy-Ochs, S., Schwartz, R., Finkel, R. C., Zimmerman, S., and Schlüchter, C.: A chronology of Holocene and Little Ice Age glacier culminations of the Steingletscher, Central Alps, Switzerland, based on high sensitivity beryllium-10 moraine dating, Earth Planet Sc Lett, 393, 220–230, https://doi.org/10.1016/j.epsl.2014.02.046, 2014.

Schlosser, O.: Geomorphologische Kartierung und glazialmorphologische Untersuchungen in der Err-Gruppe (Oberhalbstein, Kt. Graubünden), unpublished diploma thesis, Dept. of Geography, University of Zurich, 90 pp., 1990.

Schneider, S., Hoelzle, M., and Hauck, C.: Influence of surface and subsurface heterogeneity on observed borehole temperatures at a mountain permafrost site in the Upper Engadine, Swiss Alps, The Cryosphere, 6, 517–531, https://doi.org/10.5194/tc-6-517-2012, 2012.

Schwanghart, W. and Scherler, D.: Short Communication: TopoToolbox 2 – MATLAB-based software for topographic analysis and modelling in Earth surface sciences, Earth Surf Dynam, 2, 1–7, https://doi.org/10.5194/esurf-2-1-2014, 2014.

Scotti, R., Crosta, G. B., and Villa, A.: Destabilisation of creeping permafrost: The Plator rock glacier case study (central Italian Alps), Permafrost Periglac, 28, 224–236, https://doi.org/10.1002/ppp.1917, 2017.

Shewchuk, J. R.: Triangle: Engineering a 2D quality mesh generator and Delaunay triangulator, pp. 203–222, Springer, Berlin, Heidelberg, https://doi.org/10.1007/BFb0014497, 1996.

Siegfried, H.: Topographischer Atlas der Schweiz 1:25 000/1:50 000, Blatt 426: Savognin, Eidgenössische Landesopographie, Bern, 1887.

Singeisen, C., Ivy-Ochs, S., Wolter, A., Steinemann, O., Akçar, N., Yesilyurt, S., and Vockenhuber, C.: The Kandersteg rock avalanche (Switzerland): Integrated analysis of a late Holocene catastrophic event, Landslides, 17, 1297–1317, https://doi.org/10.1007/s10346-020-01365-y, 2020.

Formatiert: Deutsch (Schweiz)

Snieder, R. and Trampert, J.: Inverse problems in geophysics, in: Wavefield Inversion. International Centre for Mechanical Sciences (courses and lectures), vol 398, edited by: Wirgin, A., Springer, Vienna, 119–190, https://doi.org/10.1007/978-3-7091-2486-4_3, 1999.

Solomina, O. N., Bradley, R. S., Hodgson, D. A., Ivy-Ochs, S., Jomelli, V., Mackintosh, A. N., Nesje, A., Owen, L. A., Wanner, H., Wiles, G. C., and Young, N. E.: Holocene glacier fluctuations, Quaternary Sci Rev, 111, 9–34, https://doi.org/10.1016/j.quascirev.2014.11.018, 2015.

Solomina, O. N., Bradley, R. S., Jomelli, V., Geirsdottir, A., Kaufman, D. S., Koch, J., McKay, N. P., Masiokas, M., Miller, G., Nesje, A., Nicolussi, K., Owen, L. A., Putnam, A. E., Wanner, H., Wiles, G., and Yang, B.: Glacier fluctuations during the past 2000 years, Quaternary Sci Rev, 149, 61–90, https://doi.org/10.1016/j.quascirev.2016.04.008, 2016.

Sorg, A., Kääb, A., Roesch, A., Bigler, C., and Stoffel, M.: Contrasting responses of Central Asian rock glaciers to global warming, Scientific reports, 5, 8228, https://doi.org/10.1038/srep08228, 2015.

Springman, S. M., Arenson, L. U., Yamamoto, Y., Maurer, H., Kos, A., Buchli, T., and Derungs, G.: Multidisciplinary investigations on three rock glaciers in the Swiss Alps: Legacies and future perspectives, Geogr Ann A, 94, 215–243, https://doi.org/10.1111/j.1468-0459.2012.00464.x, 2012.

Steinemann, O., Reitner, J. M., Ivy-Ochs, S., Christl, M., and Synal, H.-A.: Tracking rockglacier activity in the Eastern Alps from the Lateglacial to the early Holocene, Quat Sci Rev, 241, https://doi.org/10.1016/j.quascirev.2020.106424, 2020.in press.

Stone, J. O.: Air pressure and cosmogenic isotope production, J Geophys Res-Sol Ea, 105, 23 753–23 759, https://doi.org/10.1029/2000JB900181, 2000.

Synal, H.-A., Bonani, G., Döbeli, M., Ender, R., Gartenmann, P., Kubik, P., Schnabel, C., and Suter, M.: Status report of the PSI/ETH AMS facility, Nuclear Instruments and Methods in Physics Research Section B: Beam Interactions with Materials and Atoms, 123, 62–68, https://doi.org/10.1016/S0168-583X(96)00608-8, 1997.

Ulrich, V., Williams, J. G., Zahs, V., Anders, K., Hecht, S., and Höfle, B.: Measurement of rock glacier surface change over different timescales using terrestrial laser scanning point clouds, Earth Surf Dynam, 9, 19–28, https://doi.org/10.5194/esurf-9-19-2021, 2021.

Vockenhuber, C., Miltenberger, K.-U., and Synal, H.-A.: ^{36}Cl measurements with a gas-filled magnet at 6 MV, Nuclear Instruments and Methods in Physics Research Section B: Beam Interactions with Materials and Atoms, 455, 190–194, https://doi.org/10.1016/j.nimb.2018.12.046, 2019.

Wicky, J. and Hauck, C.: Numerical modelling of convective heat transport by air flow in permafrost talus slopes, The Cryosphere, 11, 1311–1325, https://doi.org/10.5194/tc-11-1311-2017, 2017.

Winkler, S. and Lambiel, C.: Age constraints of rock glaciers in the Southern Alps/New Zealand – Exploring their palaeoclimatic potential, The Holocene, 28, 778–790, https://doi.org/10.1177/0959683618756802, 2018.

Wipf, A.: Gletschergeschichtliche Untersuchungen im spät- und postglazialen Bereich des Hinteren Lauterbrunnentals (Berner Oberland, Schweiz), Geogr. Helv., 56, 133–144, https://doi.org/10.5194/gh-56-133-2001, 2001.

Wirsig, C., Zasadni, J., Christl, M., Akçar, N., and Ivy-Ochs, S.: Dating the onset of LGM ice surface lowering in the High Alps, Quaternary Sci Rev, 143, 37–50, https://doi.org/10.1016/j.quascirev.2016.05.001, 2016.

Wirz, V., Gruber, S., Purves, R. S., Beutel, J., Gärtner-Roer, I., Gubler, S., and Vieli, A.: Short-term velocity variations at three rock glaciers and their relationship with meteorological conditions, Earth Surf Dynam, 4, 103–123, https://doi.org/10.5194/esurf-4-103-2016, 2016.

Zasadni, J.: The Little Ice Age in the Alps: Its record in glacial deposits and rock glacier formation, Studia Geomorphologica Carpatho-Balcanica, 41, 117–137, 2007.

Zerathe, S., Lebourg, T., Braucher, R., and Bourlès, D.: Mid-Holocene cluster of large-scale landslides revealed in the southwestern Alps by ^{36}Cl dating. Insight on an Alpine-scale landslide activity, Quaternary Sci Rev, 90, 106–127, https://doi.org/10.1016/j.quascirev.2014.02.015, 2014.